Theses and Dissertations   Student Graduate Works

3-11-2011

Passive Ranging of Dynamic Rocket Plumes using Infrared and Visible Oxygen Attenuation

Robert Anthony Vincent

Follow this and additional works at: https://scholar.afit.edu/etd

Part of the Atmospheric Sciences Commons, and the Engineering Physics Commons

www.manaraa.com

PASSIVE RANGING OF DYNAMIC ROCKET PLUMES USING INFRARED AND VISIBLE OXYGEN ATTENUATION

THESIS

R. Anthony Vincent, Captain, USAF

AFIT/GAP/ENP/11-M11

DEPARTMENT OF THE AIR FORCE
AIR UNIVERSITY

AIR FORCE INSTITUTE OF TECHNOLOGY

Wright-Patterson Air Force Base, Ohio

APPROVED FOR PUBLIC RELEASE; DISTRIBUTION UNLIMITED.

The views expressed in this thesis are those of the author and do not reflect the official policy or position of the United States Air Force, Department of Defense, or the United States Government. This material is declared a work of the U.S. Government and is not subject to copyright protection in the United States.

AFIT/GAP/ENP/11-M11

PASSIVE RANGING OF DYNAMIC ROCKET PLUMES USING INFRARED
AND VISIBLE OXYGEN ATTENUATION

THESIS

Presented to the Faculty

Department of Engineering Physics

Graduate School of Engineering and Management

Air Force Institute of Technology

Air University

Air Education and Training Command

in Partial Fulfillment of the Requirements for the

Degree of Master of Science in Applied Physics

R. Anthony Vincent, BS

Captain, USAF

March 2011

APPROVED FOR PUBLIC RELEASE; DISTRIBUTION UNLIMITED.

AFIT/GAP/ENP/11-M11

PASSIVE RANGING OF DYNAMIC ROCKET PLUMES USING INFRARED AND VISIBLE OXYGEN ATTENUATION

R. Anthony Vincent, BS
Captain, USAF

Approved:

//signed//	7 March 2011
Lt Col Michael R. Hawks (Chairman)	Date
//signed//	7 March 2011
Kevin C. Gross, PhD (Member)	Date
//signed//	7 March 2011
Michael T. Eismann, PhD (Member)	Date

Abstract

Atmospheric oxygen absorption bands in observed spectra of boost phase missiles can be used to accurately estimate range from sensor to target. One method is to compare observed values of band averaged absorption to radiative transfer models. This is most effective using bands where there is a single absorbing species. This work compares spectral attenuation of two oxygen absorption bands in the near-infrared (NIR) and visible (Vis) spectrum, centered at 762 nm and 690 nm, to passively determine range. Spectra were observed from static tests of both surface-to-air missile simulators at 405 m range and a full-scale solid rocket motor at 900 m range. The NIR O_2 band provided range estimates accurate to within 3 % for both tests, while the Vis O_2 band had range errors greater than 15 %. A Falcon 9 rocket launch at an initial range of 13 km was also tracked and observed for 90 seconds after ignition. The Vis O_2 band provided dynamic range estimates accurate to within 8 % error for the first 30 seconds of tracked observation. The NIR O_2 band, however, overestimated in-flight range with an error no less than 20 %. Rocket plumes are expected to be significantly brighter at longer wavelengths, but absorption in the NIR band is nearly ten times stronger than the Vis band, causing saturation at shorter path lengths. An atmospheric band is considered saturated when all the in-band frequencies emitted from the rocket plume are absorbed before reaching the sensor. The trade between signal to noise and saturation is discussed. Additionally, since response time is paramount for boost phase missiles defense, methods for reducing dependence on line-by-line algorithms to speed calculations are also presented.

Dedicated with love to my wife and children.

Acknowledgements

I would like to sincerely thank my adviser, Lt Col Michael Hawks, for the opportunity to work on a project with such tangible applications for security and defense. His excitement and belief in Passive Ranging was contagious. I especially appreciated his easy-going nature and persistent humor when instructing and performing research.

I also thank Dr. Kevin Gross and Dr. Michael Eismann for teaching excellent courses in spectroscopy and remote sensing, respectively. I felt very well prepared beginning my thesis research. I also thank them greatly for agreeing to be members of my thesis committee.

Finally, I would like to thank Jeremey Pitz for his hard work and expertise in ensuring successful data collection during the rocket tests. His efforts were much appreciated.

R. Anthony Vincent

Table of Contents

List of Figures

List of Tables

List of Symbols

List of Abbreviations

PASSIVE RANGING OF DYNAMIC ROCKET PLUMES USING INFRARED AND VISIBLE OXYGEN ATTENUATION

I. Introduction

The long range missile has been used in military tactics for decades. Since its inception, a tremendous effort has been made to create an adequate missile defense system. Unfortunately, such a defense system has yet to be developed. Before preventive action can be taken, the missile must first be observed with a sensor. Then estimates of position, range, and velocity can be calculated. Accurate methods to determine range to an impending missile are still under development. An important requirement to transition ranging techniques to a real world system is the ability to estimate range over a multitude of distances. Accurate estimation over long ranges is crucial for developing a robust ranging system.

Since missiles can be propelled with enormous acceleration, they can cover large distances across the globe in a matter of minutes. The most crucial moment of detection and decision is within the first few seconds of launch, during the boost phase. For detection of boost phase missiles, it is desirable that a sensor be passive (not emitting a traceable signal) to maintain a stealth signature during operations. Additionally, a single (monocular) sensor reduces the complexity of a tracking system as a whole. Finally, the algorithm to input sensed data and calculate estimates of range must be near-real-time. If the calculation of a range estimate is not a rapid process, the hostile missile may have already impacted upon its target. Therefore, the focus of this research is to investigate further into the emerging field of monocular passive ranging (MPR).

1

1.1 Previous Work

The theory of MPR began as an Air Force funded research project, led by Draper *et al*, starting approximately two decades ago, [4] . There have been several notable techniques developed over the years to estimate range, [12]. However, for the scope of this research, the focus will be primarily on the concept and development of band averaged absorption as applied to MPR.

1.1.1 Passive Ranging with Atmospheric Oxygen.

MPR using band averaged absorption was first developed at the Air Force Institute of Technology by M.R. Hawks using atmospheric oxygen absorption spectra, [7]. The oxygen spectra in the near-infrared (NIR) and visible (Vis) wavelengths are spectrally isolated from the spectral bands of other absorbing species. Additionally, since oxygen is uniformly distributed across the Earth with minimal seasonal variations, it proved to be a robust medium for applying band averaged absorption.

Hawks estimated band averaged absorption ($\bar{A}$) by making use of isolated oxygen spectra. Out-of-band data were used to fit a baseline across the absorption band, representing what the spectrum would have been without the presence of the absorption band. Therefore, the depth of the absorption band was related to the distance along the absorbing path being measured. Since column density is dependent upon both concentration and path length, the radiative transfer model, FASCODE, was used to generate transmission curves for given oxygen concentrations. From these transmission plots at varying ranges, curves of $\bar{A}$ versus range were generated for fixed altitude and zenith angles.

Data sets for passive ranging were taken of both a halogen lamp and a full scale stationary solid rocket motor at various ranges up to 3 km. Since radiative transfer models, such as FASCODE, can reference predetermined atmospheric profiles, refer-

2

enced oxygen concentrations could be corrected for with measured meteorology data. By recording the current atmospheric conditions during testing, an atmospheric correction for oxygen concentration was used to achieve range accuracy with less than 2% error.

In an effort to reduce the dimensionality and dependence upon radiative transfer methods, Hawks also investigated fitting atmospheric band models to the NIR oxygen absorption band. He demonstrated that a modified series expansion of an Elsasser or random band model could be well fit to the oxygen band. The fitting error was shown to be less than 1%. This enabled the range to $\bar{A}$ relationship to be displayed in a functional form as opposed to a computer intensive model.

1.1.2   Band Pass Filters Measuring Oxygen Absorption.

The methods developed by Hawks used frequency dependent transmission data measured by a Fourier-transform spectrometer (FTS). As FTS's demand fine precision, this makes them ill-suited for field or operational use. From this, Anderson made use of the simplicity of band averaged absorption and designed a monocular system based upon spectral filtering for the NIR oxygen band. Anderson used three spectral filters to gather two out of band measurements, one on either side, and one in band measurement [1]. He then calculated a band averaged absorption, based on the three transmitted frequencies, and determined range to target. This novel approach achieved accurate range estimates for ground based experiments with a range error of 8% – 22%. This monocular spectral filtering setup was then taken aboard a C-12 aircraft to determine range from sensor to an F-16 during afterburn. However, there was a significant amount of noise during testing and accurate range estimates were not obtained for those flight tests.

3

1.1.3 Passive Ranging with Atmospheric Carbon Dioxide.

In addition to using oxygen absorption bands, Macdonald demonstrated that band averaged absorption can be used with mid-wave infrared (MWIR) carbon dioxide, CO_2, bands to also estimate range [9]. Macdonald used archived data of bomb detonations to determine range to target over a horizontal path. The difficulty in this application was the fact that radiation from a high yield explosive was not well approximated as a blackbody radiator for calculating a band average over the CO_2 absorption band of interest. To overcome this, Macdonald incorporated previous AFIT research to determine the stoichiometry of fireballs. Additionally, since there are weak water absorption lines within the CO_2 band, a water concentration correction was also developed for increased accuracy. Once these techniques were incorporated, measurements of CO_2 transmission produced range estimates accurate to 3% for experimental data up to 5 kilometers. This technique also relied on fitting experimental data to model generated transmission curves for estimates of range.

1.2 Present Work

As demonstrated in the dissertation research of M.R. Hawks [7], the NIR oxygen absorption band can be used to accurately determine range of an emissive target up to 3 km. For surface-to-air missile (SAM) detection it may be realistic to assume a sensor will be within 3 km of a launching missile. However, for an intercontinental ballistic missile (ICBM) it is unlikely that a sensor will be within 3 km of the rocket during boost phase. With a long enough absorption path, all source photons with in-band frequencies will eventually be completely absorbed. This is considered saturation of the absorption band. When saturation occurs, accurate estimates of range are theoretically impossible. Therefore, the saturation length of an absorption band is ultimately the limiting factor in the accuracy of MPR.

4

With respect to saturation, a weaker band means a longer saturation path length. However, a weak band also produces less absorption signal over short path lengths. Therefore, there is a fundamental trade-off between absorption and saturation. In the visible spectrum, there is another oxygen absorption band that is approximately ten times weaker than the NIR oxygen band used by Hawks. Qualitatively, the stronger NIR O_2 should work better over short ranges, while the weaker Vis O_2 band should work better over longer ranges. The focus of this research is to compare the two oxygen absorption bands to determine the general range at which one O_2 band performs better than the other.

If a MPR system is desired for missile defense, then range estimates must be near-real-time. One of the problems with using a radiative transfer model for range estimation is the computational overhead required. Iterating through a complicated model until a desired accuracy is achieved can take a significant time period and requires a fast processor with adequate memory. To reduce the dependence upon iterating through a radiative transfer model, this research also investigates using pre-calculated lookup tables to enhance computation speed while introducing minimal range error.

For this research, data was taken from three different experiments where a missile or rocket propellant under combustion was targeted as the emission source. Two static tests were conducted with a full scale solid rocket motor and a shoulder-launched model SAM at distances of 900 m and 405 m, respectively. Data of a SpaceX developed Falcon 9 rocket were also taken during its launch at the Kennedy Space Center in Florida.

5

1.3 Summary

The topic of band averaged absorption as applied to monocular passive ranging is discussed in this thesis. The inclusion of the visible O_2 absorption band is evaluated and compared to the NIR O_2 band. The two are compared in order to determine the ranges and conditions in which one band generates more accurate passive range estimates than the other. Near-real-time computation techniques are also investigated and applied to a dynamic test using data taken of a Falcon 9 rocket. Chapter II discusses the theory of band averaged absorption as applied to both oxygen bands. The radiative transfer model, LBLRTM, is also discussed in this chapter, along with the conceptual development of near-real-time calculations. Chapter III discusses in detail the three experimental tests where data was taken of the emitting rocket/missile motor plumes. The test results are discussed in Chapter IV. Finally, conclusion and recommendations for future research are presented in Chapter V.

II. Theory

Earth's atmosphere is composed of many absorbing species that might be useful in spectral analysis of an emissive target. In fact, it has already been proven that both O_2 and CO_2 can be used to accurately determine range, [7], [9]. So why not use nitrogen (N_2), water (H_2O), or ozone (O_3) to estimate range? For robust measurements of range over a diverse path, an optimal spectral band should be spectrally isolated from other absorbing species. In addition, a spectral band should be distinct enough to be measured at short ranges, but not too strong so that the absorption saturates over distances typical of the experiment or application. Finally, the absorbing molecule should be uniformly distributed across the Earth with a well known altitude density profile. The latter condition is crucial if not assuming a homogeneous transmission path. It is for these reasons that the visible oxygen absorption bands are studied.

2.1 Near Infrared and Visible Oxygen Spectra

Figure 1 shows the individual line strengths and positions of the primary O_2 isotope taken from the 2008 HITRAN database [11]. The HITRAN database lists the line strengths and positions of over 1.25 million optical transitions of the 39 most common molecular species found in Earth's atmosphere. These O_2 line positions correspond to magnetic dipole transitions and are forbidden in the electric dipole approximation [2]. This means that oxygen absorption for these frequencies is rather weak and should not saturate until long atmospheric paths. The lines in the oxygen bands (Figure 1) are emission transitions from the second excited electronic state to the ground electronic state, annotated as b and X respectively. The NIR oxygen absorption band near 762nm (left side of Figure 1) is composed of several rotational transitions within the ground state vibrational levels ($\Delta v = 0$). The Vis oxygen
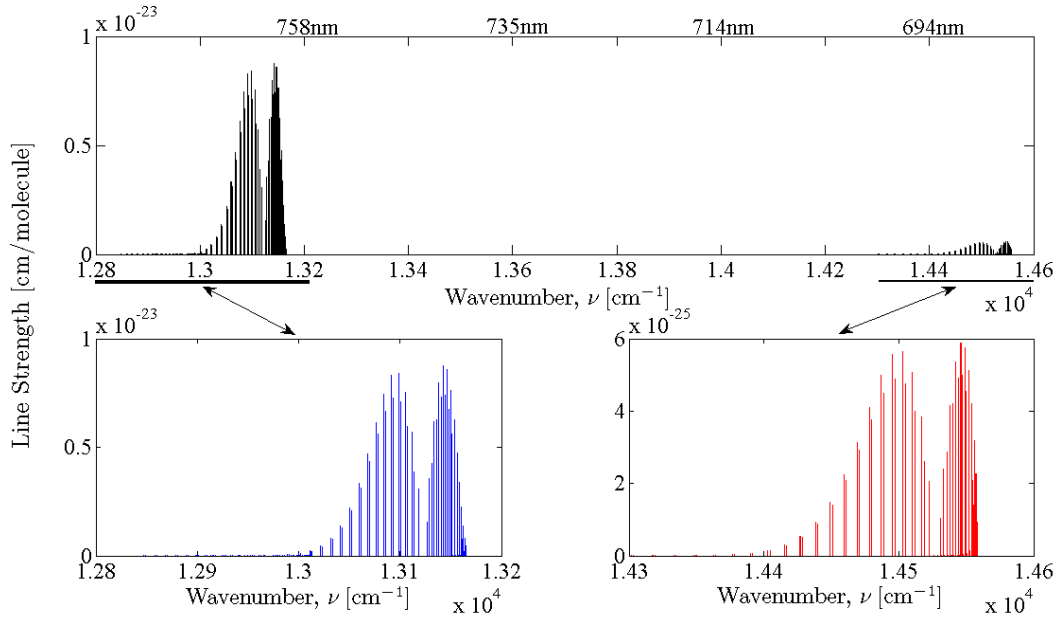
Figure 1. The individual line strengths of O_2 as taken from the HITRAN 2004 database [11]. The NIR band is displayed in blue (left) while the Vis band is shown in red (right). The NIR O_2 band is approximately ten times stronger than the visible O_2 band.

absorption band near 690nm (right side of Figure 1) contains rotational levels within the vibrational transition $v'' = 1$ to $v' = 0$ ($\Delta v = 1$).

Both oxygen absorption bands have the common form of distinct P and R branches associated with vibrational-rotational bands [2]. However, complexity is added by the fact that these are magnetic dipole and not electric dipole transitions. Upon closer inspection, each line has a closely spaced doublet line of slightly different intensity separated by approximately $4\,\mathrm{cm}^{-1}$. It is also worth noting that the Vis O_2 band has the same shape and form as the NIR O_2 band, but is roughly 10 times weaker. These quantitative spectral features of oxygen are key ingredients for tailoring a useful band model to determine range.

8

2.2 Band Average Absorption

2.2.1 Derivation.

The theory of MPR is based upon measuring the electromagnetic radiation emitted from a target over a certain frequency spectrum and using the amount of radiation absorbed by the atmosphere to estimate range. The earliest work in MPR assumed the most simplistic of cases, that absorption follows Beer's Law:

$$dI = -k(\nu)Idl, \tag{1}$$

where k is the absorption coefficient and a function of temporal frequency ν and I is the source intensity emitted along an incremental path dl, [4]. The Beer's Law solution to this differential equation assumes that k is independent of position, which leads to the well known result,

$$I = I_0 e^{-k(\nu)L}, \tag{2}$$

where I_0 is the initial source intensity and L is the total path length (range) [7],[10].

For non-idealistic settings k can not be assumed a constant of position to good approximation when light is propagating through the Earth's atmosphere. Neglecting extinction from scattering, k can be expressed as the product of the cross-section of absorption (σ) and the number density of the absorber (N) [7],[10],

$$k(\nu, l) = \sigma(\nu, l)N(l). \tag{3}$$

The density of elements and molecules in the atmosphere varies significantly with temperature and altitude [8]. Also, σ is dependent upon the line shape of the energy transition in the molecule. Line shape can be accurately described by a Lorentzian, Gaussian, or Voight profile depending upon the temperature and pressure of the ab-

9

sorbing molecule. Therefore, both σ and N vary with altitude and position. However, the functional form of k with respect to altitude is often approximated as a constant over the observed path.

Another added complexity to the Beer's Law assumption is that a real world sensor does not measure a monochromatic frequency, ν. The intensity recorded at a certain frequency will actually be an average over the spectral resolution band of that instrument. It was to this effect that Hawks developed a band averaged absorption approach using the oxygen absorption band centered at $13,120\,\mathrm{cm}^{-1}$ or $762\,\mathrm{nm}$ in the NIR, referred to as the NIR O_2 band. This technique uses the out-of-band data to generate a baseline intensity across the absorption band representing the spectral intensity of a Planckian distribution in the absence of the absorption band. The band averaged transmission, $\bar{T}$, is then defined to be

$$\bar{T}(\nu) = \frac{\bar{I}(L)}{\bar{I}_0} = \frac{1}{\Delta\nu}\int T(\nu)d\nu = \frac{1}{\Delta\nu}\int_{\nu_i}^{\nu_f} \exp(-\tau_\nu)d\nu, \tag{4}$$

where T is the monochromatic transmission and τ is the monochromatic optical depth,

$$\tau(\nu) = \int_0^L k(\nu, l)dl. \tag{5}$$

For rocket plumes during combustion, it is safe to assume that reflections off the plume are negligible. Therefore, band average absorption $(\bar{A})$ is simply related to band average transmission by the relation,

$$\bar{A} = 1 - \bar{T}. \tag{6}$$

By using out-of-band data to fit a baseline across the absorption band, equation (6)

10

can be expressed in discrete notation as the working equation,

$$\bar{A} = 1 - \frac{\sum_{\nu_i}^{\nu_f} I(\nu)}{\sum_{\nu_i}^{\nu_f} I_b(\nu)} \approx 1 - \frac{\sum_{\nu_i}^{\nu_f} T(\nu)}{\sum_{\nu_i}^{\nu_f} T_b(\nu)}, \tag{7}$$

where the subscript b denotes an interpolated baseline value. Here ν_i and ν_f define the in-band frequencies of consideration. Discrete notation is used to point out the numerical aspect of the calculation. It is worth noting that equation (7) neglects path radiances scattered into the observation path. It is possible to model path radiances. However, path radiances are highly dependent upon knowing the geometry of the sun with respect to the sensor and are also affected by the density and type of clouds in the local atmosphere. So far, evidence suggests that path radiances are often negligible when observing rocket emission plumes.

2.2.2 Treatment of Uncertainty.

A starting point for characterizing the uncertainty in equation (7) is to first assume that the uncertainties in I and I_b are independent and random. Since the summations in equation (7) contain the same number of frequency samples for both the numerator and denominator, this equation can be rewritten as

$$\bar{A} = 1 - \frac{\bar{I}}{\bar{I_b}}, \tag{8}$$

where the over-set bar represents an in-band arithmetic mean. The generalized method for calculating the uncertainty in $\bar{A}$ ($\sigma_{\bar{A}}$) as a function of several variables is expressed as

$$\sigma_{\bar{A}} = \sqrt{\left(\frac{\partial \bar{A}}{\partial \bar{I}} \sigma_{\bar{I}} \right)^2 + \left(\frac{\partial \bar{A}}{\partial \bar{I_b}} \sigma_{\bar{I_b}} \right)^2}, \tag{9}$$

11

where σ represents a standard deviation about its mean value, [13]. After calculating the partial differentials of equation (8), the standard deviation for $\bar{A}$ takes the form

$$\sigma_{\bar{A}} = \sqrt{\left(\frac{-1}{\bar{I}_b} \times \sigma_{\bar{I}}\right)^2 + \left(\frac{\bar{I}}{\bar{I}_b^2} \times \sigma_{\bar{I}_b}\right)^2} = \frac{1}{\bar{I}_b}\sqrt{\sigma_{\bar{I}}^2 + \left(\frac{\bar{I}}{\bar{I}_b}\right)^2 \sigma_{\bar{I}_b}^2}. \qquad (10)$$

Note that the mean in-band observed radiance divided by the mean baseline value is simply one minus band averaged absorption. Using this fact, the above equation can be simplified further to produce the following result,

$$\sigma_{\bar{A}} = \frac{1}{\bar{I}_b}\sqrt{\sigma_{\bar{I}}^2 + \left(1 - \bar{A}\right)^2 \sigma_{\bar{I}_b}^2}. \qquad (11)$$

Care must be taken when calculating the standard deviations of the in-band and baseline radiances, $\sigma_{\bar{I}}$ and $\sigma_{\bar{I}_b}$ respectively. A direct calculation of $\sigma_{\bar{I}}$ can not be accomplished without prior knowledge of the true shape of the absorption band. To remedy this, $\sigma_{\bar{I}}$ is assumed to be approximately equal to the standard deviation of the out-of-band radiances. $\sigma_{\bar{I}}$ is then calculated spectrally by fitting a low order polynomial through the out-of-band data. The polynomial line is subtracted from the out-of-band signal and the standard deviation of the resulting zero mean spectrum is taken to be $\sigma_{\bar{I}}$. Additionally, $\sigma_{\bar{I}_b}$ is not a straight forward calculation either. A built-in Matlab function for polynomial fitting was used to calculate $\sigma_{\bar{I}_b}$. The details of implementing this procedure numerically are shown in the Matlab code presented in Appendix A.

2.3   Line By Line Radiative Transfer Model

2.3.1   Description of Algorithm.

The Line By Line Radiative Transfer Model (LBLRTM) is a radiative transfer algorithm that uses the HITRAN database to compute high resolution optical depths, [3], [11]. Since LBLRTM computes a Voight line-shape profile for every spectral line listed in the desired frequency range, it is therefore considered a "line-by-line" algorithm. The spectral resolution benefit from performing a line-by-line calculation comes at the cost of increased computation time. Most of the computational overhead is used to approximate the convolution of the homogeneously broadened line-shape with the inhomogeneous Doppler line-shape, [2]. LBLRTM also includes calculations for extinction due to Rayleigh scattering. The error of the LBLRTM algorithm has been calculated to be approximately 0.5%, which is on the order of five times less than the error associated with the line parameters themselves, [3].

It is possible to input a user defined atmospheric profile into LBLRTM. However, there are several commonly used atmospheric profiles preloaded into the algorithm, such as arctic, mid-latitude, tropical, and the 1976 U.S. Standard Atmosphere. For the research presented in this thesis, the 1976 U.S. Standard Atmosphere was used in all model runs of LBLRTM, [8]. Additionally, there are numerous input parameters available to customize a particular atmospheric path. Most of the available parameters were left in their default setting for this study (see Appendix D), while the three varied were path length (range), zenith angle along the slant path, and observer altitude.

Figure 2 displays the 1976 Standard Atmosphere concentration profiles on a logarithmic y-axis for oxygen, carbon dioxide, and water. Figure 2 shows that both O_2 and CO_2 closely resemble a decaying exponential profile. This fact is crucial for using an absorbing species in various viewing geometries for accurate passive ranging. The
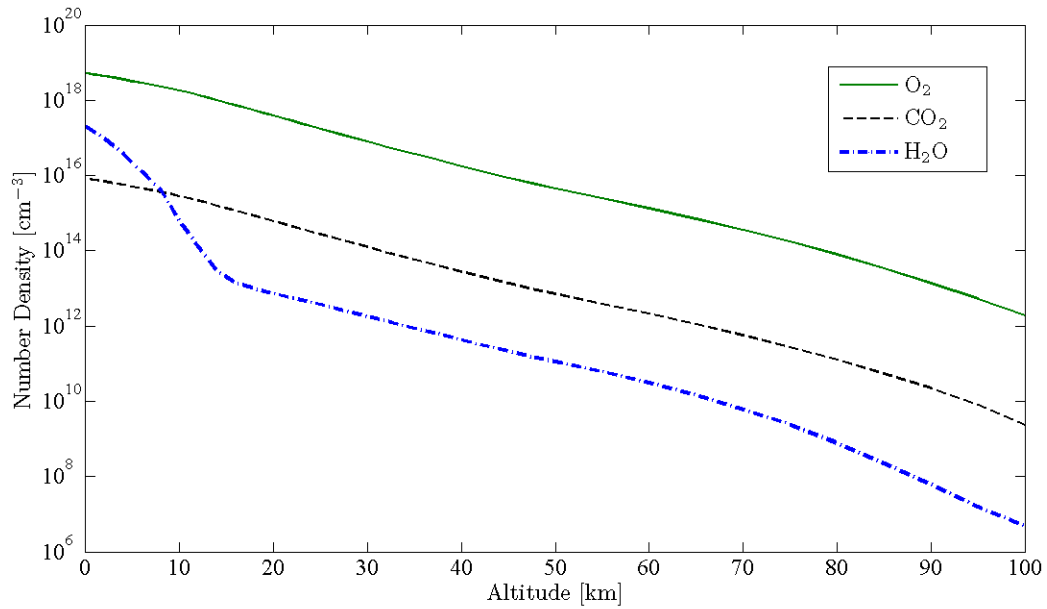
Figure 2. The number density altitude profiles of O_2, CO_2, and H_2O used in the U.S. 1976 Standard Atmosphere. Number density is displayed with a logarithmic axis. Both O_2 and CO_2 closely resemble an exponential decaying function, while H_2O does not. The tropopause can be seen in the H_2O profile near 13 km.

H_2O concentration profile is more difficult to describe, because it is highly dictated by the location of the tropopause. Since the tropopause varies significantly with latitude, it is advantageous to avoid H_2O absorption lines altogether when calculating passive range estimates.

2.3.2 Range Estimation.

Since $\bar{A}$ is the observable metric, a functional relationship between $\bar{A}$ and range must be established in order to estimate range. To create a curve of $\bar{A}$ versus range, LBLRTM was used to generate transmission plots at varying ranges for a fixed sensor altitude and zenith angle. The fidelity of the absorption range curve is dependent upon the range increments at which the model is run. More modeled range points leads to a better description of the absorption versus range behavior. However, run-

ning LBLRTM takes computation time and memory, so there needs to be a balance between curve accuracy and run time.

Figure 3 shows the LBLRTM transmission plot for the NIR O_2 band at a 1 km path length, while Figure 4 shows the same band at 300 km. These plots were generated with an 89 deg zenith angle and a one kilometer ground level altitude. To be discussed in the next chapter, there are often two strong potassium emission lines present in the spectra of rocket combustion sources that fall in the P-branch of the NIR O_2 band. These emission lines are specific to the observed combustion and are therefore not modeled in LBLRTM. Because of this, only the R-branch of this band will be used for passive ranging. Figures 3 and 4 show that this band is indeed spectrally isolated from other atmospheric species. It is important to note that for an 89 deg zenith angle the R-branch is strongly saturated at 300 km, while at 1 km $\bar{A}$ varies with range. This shows that for a zenith angle near 90 deg, the NIR band is strong enough to absorb nearly all of the emitted in-band frequency photons along a sufficiently long observation path within the atmosphere.

Figures 5 and 6 display transmission plots of the Vis O_2 band for the same conditions as in Figures 3 and 4. The Vis O_2 band is not as spectrally isolated as the NIR O_2 band. There is a weak water band that slightly overlaps with the P-branch of the Vis O_2 spectra. For this reason, the P-branch of the Vis O_2 band was not used for passive ranging. Only the R-branch remains isolated enough for accurate range estimates, without correcting for water concentrations. Also, Figure 6 shows that for a 300 km path length and an 89 deg zenith angle, the Vis O_2 band is not saturated.

Once transmission is modeled, $\bar{A}$ can be calculated by fitting a low order polynomial through out-of-band frequencies. This creates a best fit baseline value across the absorption band. Then equation (7) is used to calculate $\bar{A}$ for the in-band data, in this case, the R-branch of the oxygen bands. Figures 3-6 display the resulting

15

Table 1. Wavenumber values used to compute in-band and out-of-band ranges for the NIR and Vis O_2 bands.

O_2 band	$\Delta\nu_{out,1}$ (cm^{-1})	$\Delta\nu_{in}$ (cm^{-1})	$\Delta\nu_{out,2}$ (cm^{-1})
NIR	$12785 - 12843$	$13122 - 13200$	$13200 - 13360$
Vis	$--$	$14527 - 14566$	$14590 - 14900$

interpolated baselines as a dashed red line. Table 1 shows the frequency ranges used for out-of-band and in-band data for both NIR and Vis O_2 bands. There is only one out-of-band data range for the Vis O_2 band, because there is an extending water band running next to the Vis P-branch. This one-sided baseline extrapolation is not as accurate as bracketing the in-band data, as with the NIR O_2 band. However, this baseline error is expected to be much smaller than the error associated with weaker absorption.

By varying range, running LBLRTM, and calculating $\bar{A}$, an absorption versus range curve is generated for a given altitude and zenith angle. Figure 7 shows an $\bar{A}$ curve for both NIR and Vis bands, with an altitude of approx 1 km and a zenith angle of 89 deg. The solid circles represent the point at which $\bar{A}$ is 90% of its value at a range of 300 km. Therefore, the solid circles in Figure 7 relate to range values of 90% saturation for the given geometry. Figure 7 shows that the Vis O_2 band has a saturation length around three times longer than that of the NIR band.

Figure 8 also displays the curves of $\bar{A}$ versus range, but for the three zenith angles of 0, 45, and 89 deg. The NIR O_2 band is depicted in blue, while the Vis band is depicted in red. This shows that for both O_2 bands, the atmosphere runs out well before saturation due to absorption, until the zenith angle approaches 90 deg. Therefore, the possible benefit of using the weaker Vis O_2 band will only be realized when looking through zenith angles near 90 deg, where there are dense columns of atmosphere. For zenith angles less than 45 deg, the NIR band is expected to always yield better range estimates than the Vis band. This is simply because the atmosphere

16
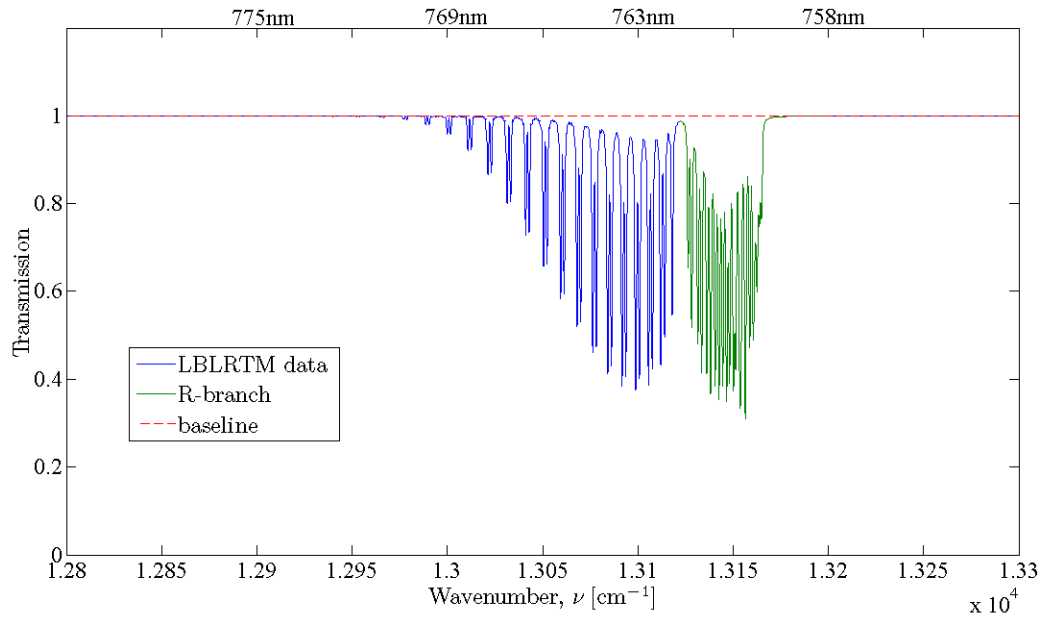
Figure 3. Transmission plot for the NIR O_2 band generated by LBLRTM for a range of 1 km, zenith angle of 89 deg, and altitude of 1 km. The R-branch, used as the in-band data, is shown in green, while the interpolated baseline is displayed as the dashed red line. For Figures 3−6 the displayed spectrum was generated by convolving the line-by-line spectrum with a 1 cm^{-1} line shape function.
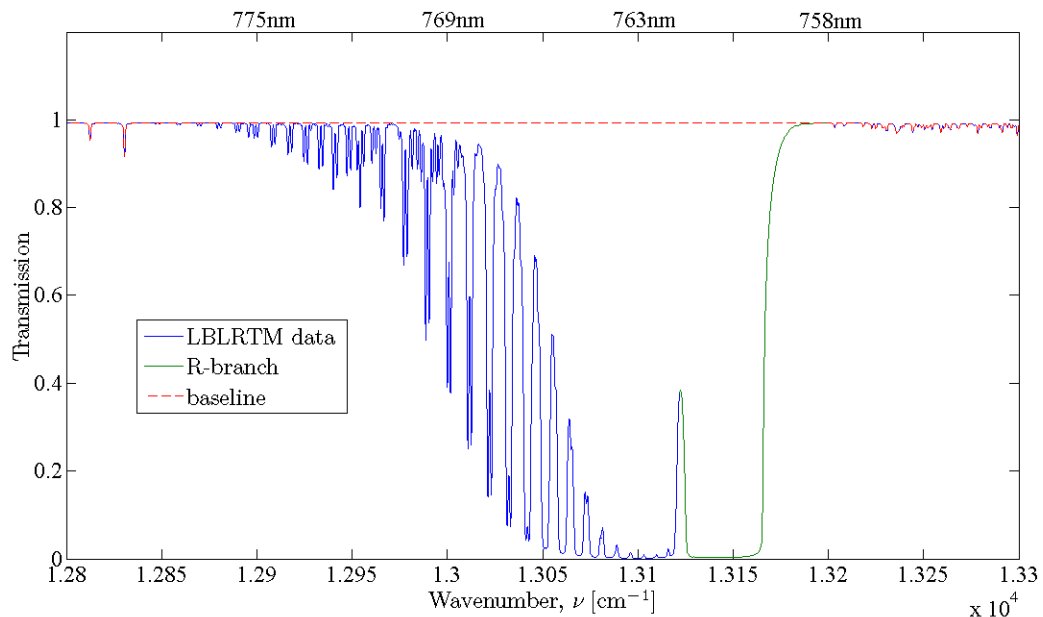
Figure 4. Transmission plot for the NIR O_2 band generated by LBLRTM for a range of 300 km, zenith angle of 89 deg, and altitude of 1 km. The R-branch, used as the in-band data, is shown in green, while the interpolated baseline is displayed as the dashed red line. Notice that the R-branch is completely saturated.

17
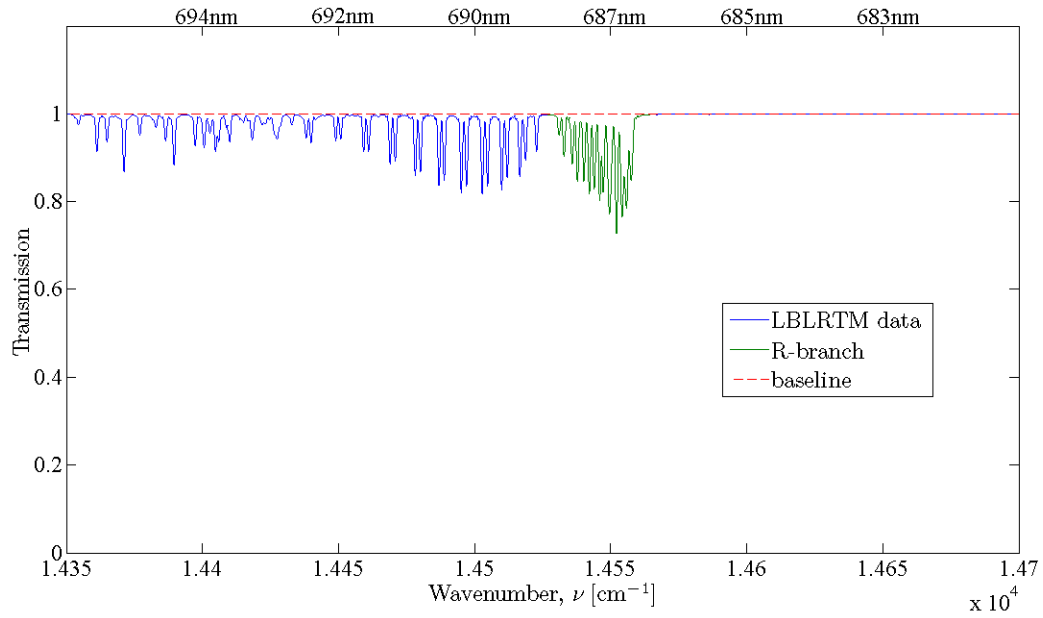
Figure 5. Transmission plot for the Vis O_2 band generated by LBLRTM for a range of 1 km, zenith angle of 89 deg, and altitude of 1 km. The R-branch, used as the in-band data, is shown in green, while the interpolated baseline is displayed as the dashed red line.
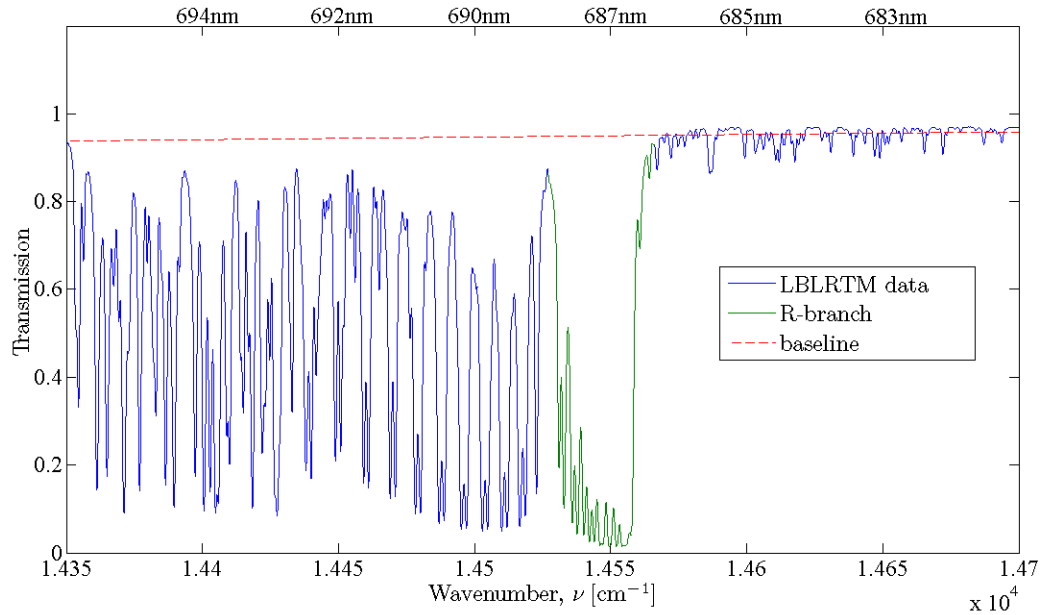
Figure 6. Transmission plot for the Vis O_2 band generated by LBLRTM for a range of 300 km, zenith angle of 89 deg, and altitude of 1 km. The R-branch, used as the in-band data, is shown in green, while the interpolated baseline is displayed as the dashed red line. Note the water spectral lines overlapping with the P-branch for this O_2 band.
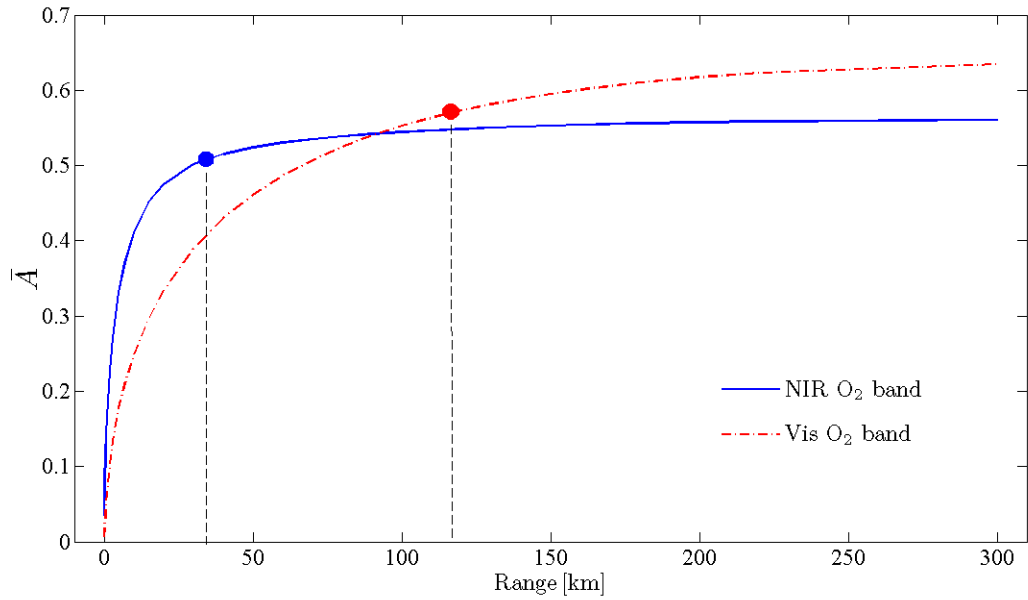
Figure 7. LBLRTM generated curve of band averaged absorption versus range for a zenith angle of 89 deg and an altitude of 1 km. Thirty transmission plots were modeled at various ranges to generate this curve. The solid circles represent the value of $\bar{A}$ that is 90% of its value at 300 km.
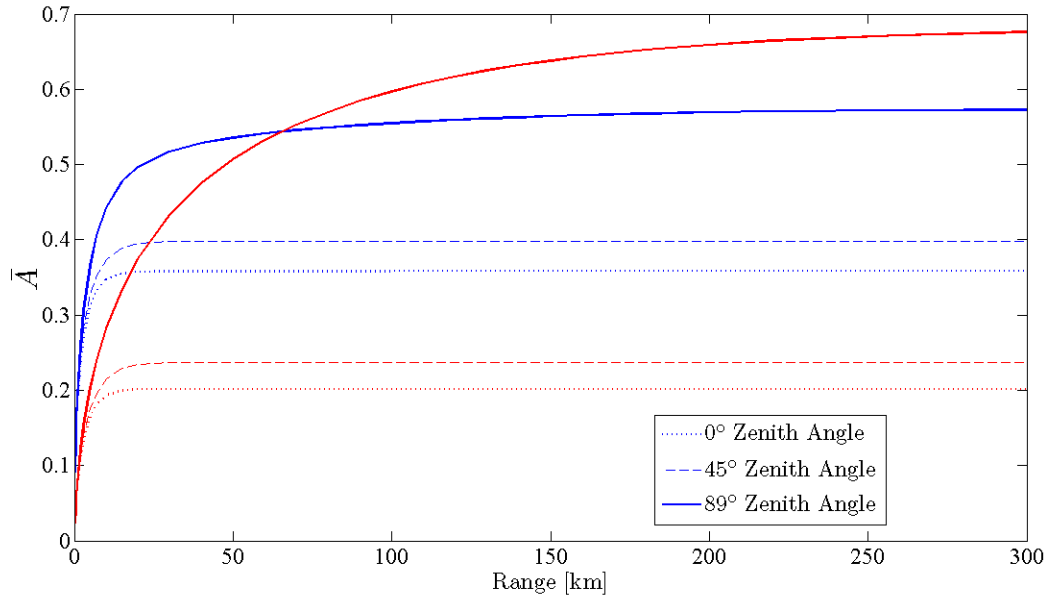
Figure 8. LBLRTM generated curves of band averaged absorption versus range for zenith angles of 0 deg (dotted), 45 deg (dashed), and 89 deg (solid), with an altitude of 1 km. The blue lines represent the NIR O_2 band while the red lines represent the Vis O_2 band.

19

will be the limiting factor and the NIR band will have greater absorption for a higher signal.

Finally, variations between the actual O_2 concentration profile and the referenced model profile should be minimized in order to accurately estimate range. Discrepancies between the two profiles translates monotonically into range error. A guaranteed method for matching the model O_2 profile to the observed profile would be to directly measure the O_2 column density through an atmospheric sounding. However, for a fieldable MPR system, atmospheric soundings may not be feasible or available in deployed locations. Additionally, if an atmospheric sounding apparatus was designed into the MPR platform it would defeat the tenet of passive sensing, because a sounding is inherently based upon active measurements.

Therefore, a method for employing a concentration correction based upon an ideal gas approximation has been shown to produce accurate range estimates for small profile variations, [1, 7, 9]. The O_2 concentration (n) at the sensor is easily determined from measuring pressure (P) and temperature (T). By assuming a small linear correction for range, an atmospheric range correction parameter (C_R) is therefore defined to be

$$C_R = \frac{n_{obs.}}{n_{ref.}} \approx \frac{P_{obs.}}{k_B \times T_{obs.} \times n_{ref.}}, \tag{12}$$

where k_B is Boltzmann's constant, the subscript *obs.* denotes a measured value at the sensor, and the subscript *ref.* signifies a value referenced by LBLRTM. A corrected range estimate is then provided by the product of the range correction parameter and the raw range estimate,

$$R_{est.} = C_R \times R_{raw}. \tag{13}$$

A detailed discussion of the validity and motivation of this method is provided in reference [7].

Table 2. Two dimensional conceptual lookup table for $\bar{A}$, varying with zenith angle (ϕ) and range (R). Created for a fixed sensor altitude above sea level (Z_f).

Z_f	R_1	R_2	R_3	R_4	...
ϕ_1	$\bar{A}_{11}$	$\bar{A}_{12}$	$\bar{A}_{13}$	$\bar{A}_{14}$	...
ϕ_2	$\bar{A}_{21}$	$\bar{A}_{22}$	$\bar{A}_{23}$	$\bar{A}_{24}$	...
ϕ_3	$\bar{A}_{31}$	$\bar{A}_{32}$	$\bar{A}_{33}$	$\bar{A}_{34}$	...
ϕ_4	$\bar{A}_{41}$	$\bar{A}_{42}$	$\bar{A}_{43}$	$\bar{A}_{44}$	...
...	...	...	...	...	...

2.4   Near-Real-Time Range Estimation

Since line-by-line calculations are so computationally intensive, it was not until the invention of the modern computer that they were even possible. Prior to line by line calculations, atmospheric band models were fit to empirical data in order to relate optical depth to path length. This created an approximated functional form that could be easily calculated and inverted. However, the accuracy of atmospheric band models over diverse locations and geometry is less than that of line by line calculations, [5, 6, 14].

For the work presented in this thesis, a 64-bit computer with dual-core 2 GHz processors was used for all computations and model runs. It took an average of 4.3 seconds of computer time to generate one transmission plot for the given frequency ranges in Table 1. Therefore, to generate one estimate of range based on 30 LBLRTM sampled data points, it took 130 seconds of computational time. This is a significant time lag for boost-phase missile defense. In two minutes a ballistic missile launching from sea level would be well into the troposphere before one estimate of range could be generated.

In order to reduce the computation time of post acquisition, it is possible to pre-calculate $\bar{A}$ values for numerous LBLRTM parameters. Given that the three most influential parameters in LBLRTM are altitude, range, and zenith angle, a lookup

21
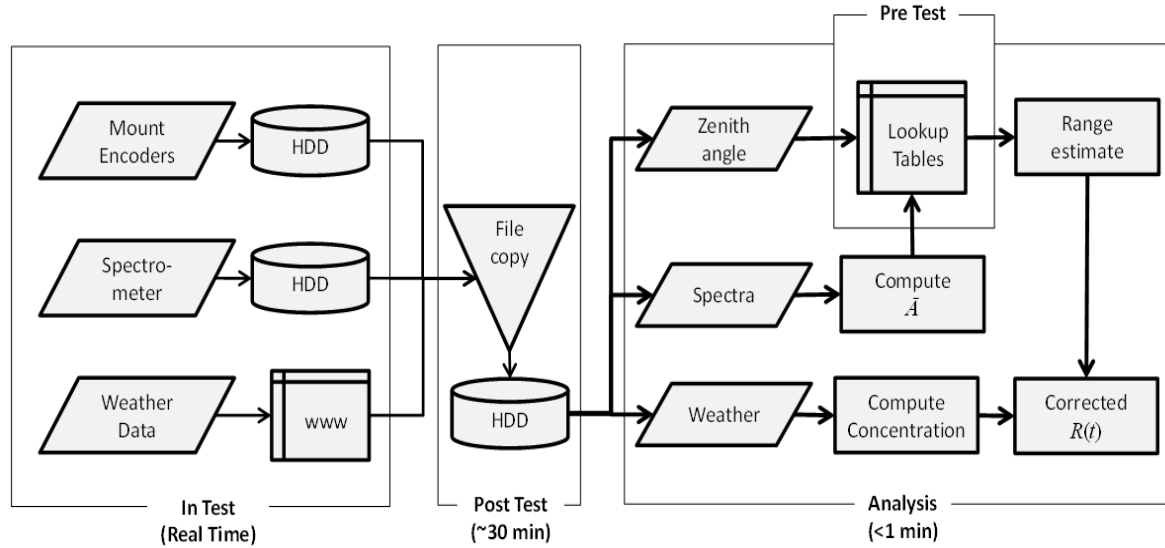
Figure 9. Conceptual block diagram displaying the data flow from sensor acquisition to range estimation. It is assumed that the in-test and post-test blocks are fixed processes, while the analysis blocks are free to be optimized for near-real-time range estimation.

table can be created for various zenith angles and ranges with a fixed sensor altitude. Table 2 shows a conceptualization of such a lookup table where the sensor altitude (Z) is a fixed value, and $\bar{A}$ is calculated for various modeled scenarios of zenith angle (ϕ) and range (R). It is assumed in this work that atmospheric concentrations are not dependent upon azimuth angle. Therefore, an isotropic atmosphere is assumed for a given zenith angle.

Considering observation using laboratory optics and hardware, there may be limited control over the speed and mechanism in which spectral data is collected and stored. However, once the data is available for analysis it can be optimized and timed for extrapolating to an operational near-real-time MPR system. Figure 9 shows a block diagram of the data flow starting with acquisition of the emitted spectra, sensor pointing data, and weather data. The raw data is then consolidated on a hard drive after the test and considered available for analysis. Then a range estimate is rapidly calculated by using the predetermined lookup table shown in Table 2.

22

2.5 Space Shuttle Trajectory Predictions

A well known Space Shuttle trajectory, from Kennedy Space Center to the International Space Station, is used to predict the behavior of band averaged absorption from a generalized rocket launch. This prediction assumes a stationary sensor on a pivoting mount capable of tracking the duration of the launch. The sensor is located 16 km from the launch site with assumed clear skies. Figure 10 shows the time evolution of azimuth and zenith looking angles (degrees) of the Shuttle from takeoff, $Time = 0$ min. The zenith angles in Figure 10 show that a minimum of 54 degrees is quickly reached within two minutes of blastoff. Range from sensor to Shuttle is given in Figure 11. This figure shows that the Shuttle range reaches 300 km in a little over four minutes.

A sea level altitude is considered for this scenario, given that Kennedy Space Center is located on the East coast of Florida. A 2-d lookup table, as described in the previous section, is generated by looping LBLRTM over various range values, zenith angles, and calculating $\bar{A}$ for each run (Appendix B & D). The surface plots in Figures 12 and 13 are the resulting lookup tables for the NIR O_2 and Vis O_2 bands, respectively. 30 range points and 19 zenith angles were considered, and are displayed as the solid black grid lines on the surface plots. The range values start at 100 meters and go up to 300 km, with greater sampling fidelity at the closer ranges. The zenith angles increment with near even steps of 5 degrees, starting at 1 degree and ending at 89 degrees.

The dashed lines with direction arrows in Figures 12 and 13 show the predicted $\bar{A}$ values for each oxygen band during launch. These projections were calculated by using the known range and zenith angles and then interpolating the value of $\bar{A}$ from the surface plots. Saturation of $\bar{A}$ with respect to range can either be due to saturation in the absorption band or a depletion of oxygen from a decreasing

exponential atmospheric profile. Either cause degrades the ability to estimate range. When the slope of $\bar{A}$ with respect to range approaches zero, measurements of $\bar{A}$ approach an asymptotic value of maximum absorption. As $\bar{A}$ values approach this saturation asymptote, small increases in $\bar{A}$ translate to extremely large increases in range. Eventually, this leads to range values that blow-up towards infinity. Therefore, there must be a nonzero slope to achieve accurate range estimates.

Figure 14 is a plot of the partial derivative of $\bar{A}$ with respect to range for the given trajectory of the Shuttle launch. This figure shows that a minute and a half into flight the slope of $\bar{A}$ is close to zero for both bands. Figure 14 also shows that the Vis O_2 band starts with twice the slope of the NIR O_2 band. Thus, if signal to noise ratio (SNR) values for each band are equal, it could be expected that the Vis band would produce more accurate range estimates in the first minute of flight than the NIR band. However, since rocket plumes radiate roughly as black bodies of a few thousand degrees, the Vis band is expected to have less signal than the NIR band. In conclusion, the interplay between $\bar{A}$ slope and SNR should be measured empirically to determine which effect wins out for most accurate range estimates.

2.6   Summary

For applications of MPR, the NIR and Vis oxygen bands are desirable candidates for computing band averaged absorption. This is because they are spectrally isolated and mixed throughout the atmosphere with an approximate exponential profile. The NIR O_2 band is theorized to generally yield better estimates of range from sensor to target over near ranges, while the Vis O_2 band is theorized to give better range estimates over longer observation paths near the horizon. The exact range at which this trade-off occurs has yet to be determined and may be specific to the scenario in which the data is collected.

24
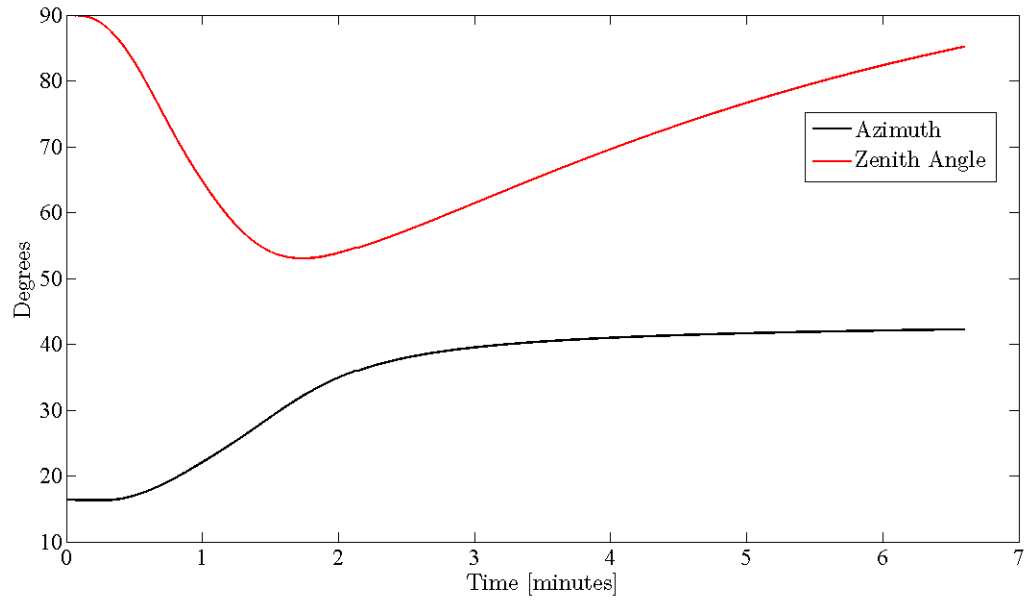
Figure 10. Predicted values of zenith and azimuth angles for a Space Shuttle to International Space Station launch. The sensor is taken to be at sea level and 16 km away from the launch pad. Blastoff occurs at time $T = 0$ minutes.

Band averaged absorption is calculated by fitting a low order polynomial baseline through out-of-band frequencies, interpolating the baseline across the in-band absorption feature, and computing the fraction of the area removed from the spectrum by the absorption band. A radiative transfer model, such as LBLRTM, can then be used to equate $\bar{A}$ values to ranges along an observation path. To speed up the analysis process for estimating range, a pre-calculated two dimensional lookup table of $\bar{A}$ can be used for incremental zenith angles and ranges. The next chapter discusses static and dynamic range experiments conducted using the procedures outlined in this chapter.

25
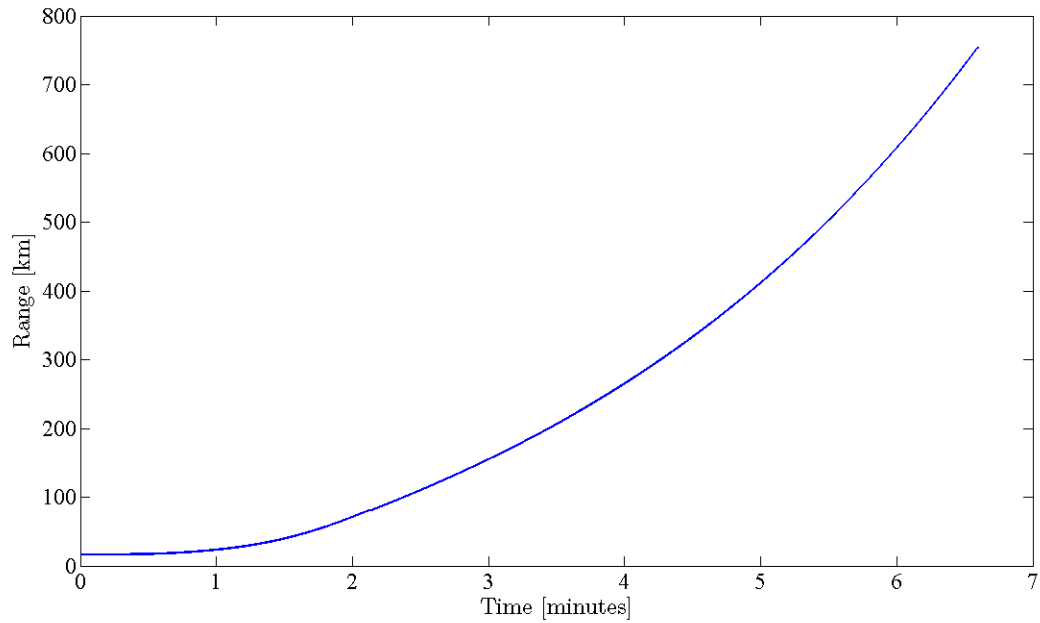
Figure 11. Predicted range progression from sensor to Space Shuttle. The sensor is taken to be at sea level and 16 km away from the launch pad. Blastoff occurs at time $T = 0$ minutes.
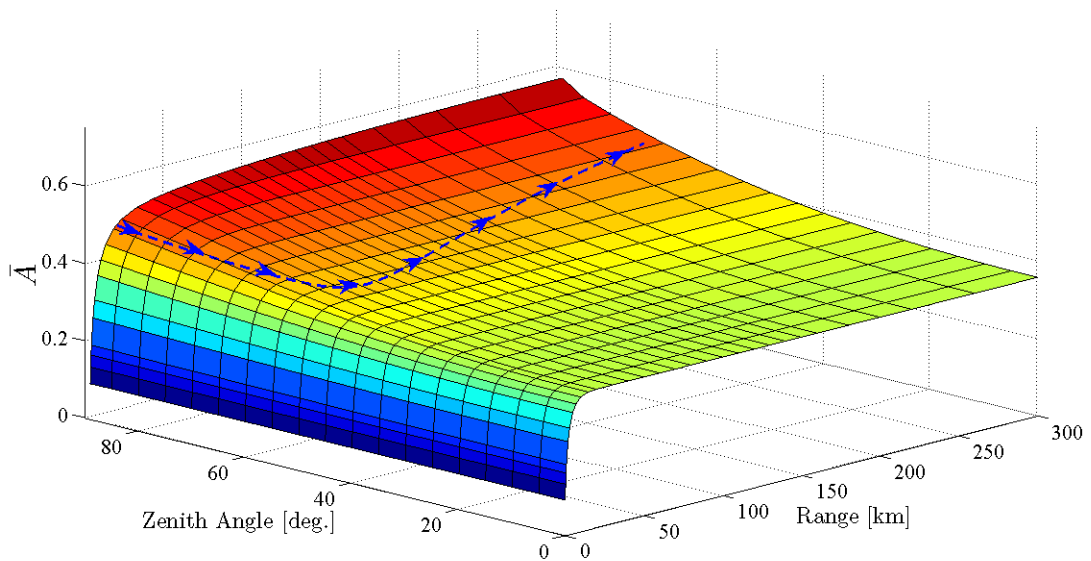
Figure 12. Surface plot of the $\bar{A}$ lookup table for the NIR O_2 band using a 1976 U.S. Standard Atmospheric profile. The sensor altitude is assumed to be at sea level. The dashed line with directional arrows represents the predicted absorption path a Space Shuttle would take during launch.

26
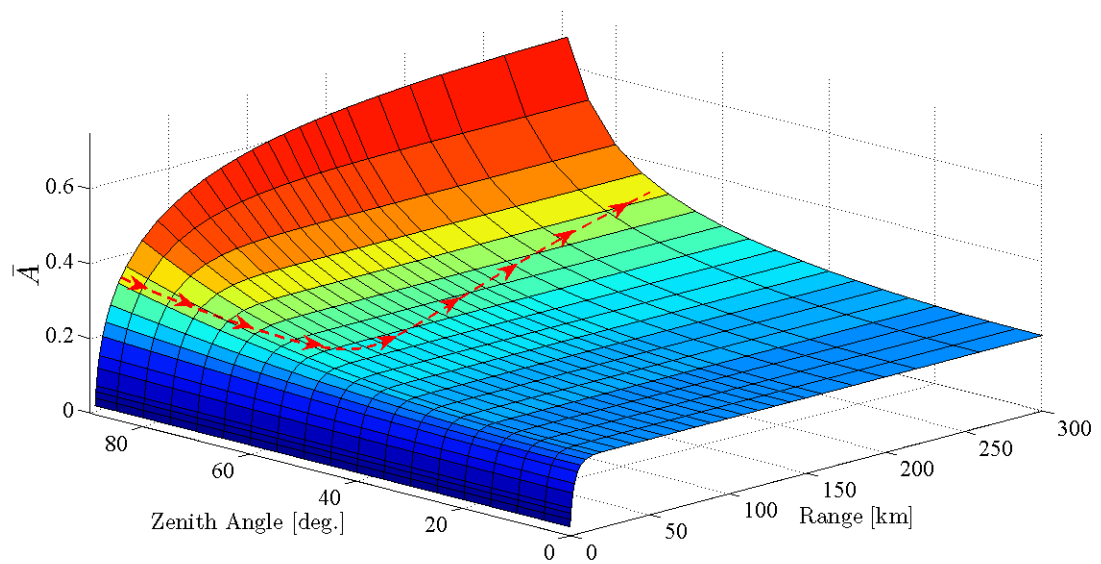
Figure 13. Surface plot of the $\bar{A}$ lookup table for the Vis O_2 band using a 1976 U.S. Standard Atmospheric profile. The sensor altitude is assumed to be at sea level. The dashed line with directional arrows represents the predicted absorption path a Space Shuttle would take during launch.
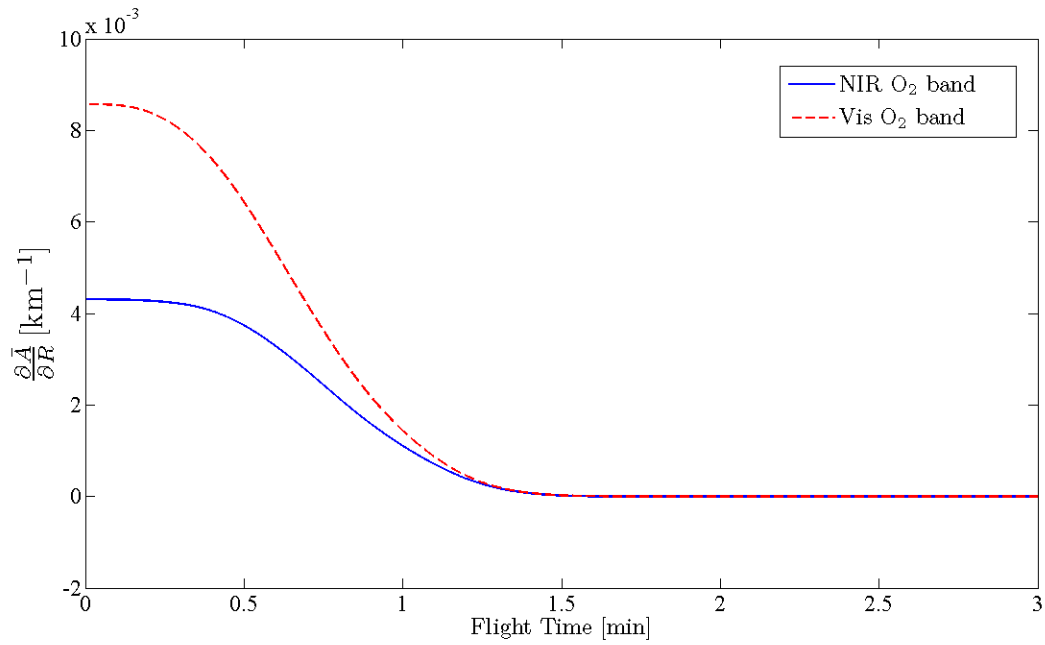
Figure 14. The predicted slope of $\bar{A}$, with respect to range $(\partial\bar{A}/\partial R)$, for a Space Shuttle launch to the International Space Station. Notice that the initial slope of $\bar{A}$ for the Vis O_2 band is twice that of the NIR O_2 band. The slope for both bands quickly falls off towards zero after the first minute of launch.

III. Experiments

For experimental verification of the theory of band averaged absorption, it is desirable to design tests that closely mimic the intended operational scenario. In this case, emissive targets were limited to combustion sources found in common rocket or missile motors. Rocket and missile tests are not easy to schedule and attend, because of safety and monetary barriers. Over the course of one year three such tests were successfully observed and are reported in this thesis: a static miniature model SAM at 405 meters, a full scale static solid rocket motor at 900 meters, and a tracked Falcon 9 rocket launch with an initial range of 13 km.

3.1 Instrumentation

All the data of the NIR and Vis spectrum from emissive targets were taken with a single field-portable Bomem spectrometer. The ABB-Bomem MR-304, hereby referred to as the MR-304, is a Fourier-transform spectrometer based upon a traditional Michelson interferometer. The MR-304 has an interferogram collection frame rate between $10 - 107$ Hz. These rates correspond, respectively, to user defined spectral resolutions between 1 and $32 \, \text{cm}^{-1}$ and are selectable in powers of two. There are two separate channels on the MR-304, enabling simultaneous operation of the Si $(0.63 - 1.0 \, \mu\text{m}$, channel A) and InGaAs $(0.8 - 1.6 \, \mu\text{m}$, channel B) detectors. The total acquisition spectral range is between $6,000 - 16,000 \, \text{cm}^{-1}$.

Each detector voltage is sampled by a 16-bit analog to digital converter (ADC) with gain settings of $1 - 64$, also selectable in powers of two. The ADC is set to digitize voltages between ± 2.5 V. There is also an optional auto-gain setting in which the software controller optimizes gain according to the detector voltage. When using auto-gain, there is a slight temporal lag of a few frames as the gain adjusts to a time

29

Figure 15. Picture of the Bomem MR-304 with attached 4.9 mrad Cassegrain telescope. This picture shows the MR-304 mounted on a Quickset gimbal for sensor pointing and target acquisition. This was the setup used for the Smoky SAM test.

changing emissive target.

A choice of three telescopes enable an instrument full field of view (FOV) of 76, 28, or 4.9 mrad with corresponding minimum focal distances of 2, 10, and 30 m. At 1 km, the diameter of the circular FOV will be one of 76, 28, or 4.9 m. Figure 15 shows a picture of the MR-304 with the 4.9 mrad Cassegrain telescope attached to the input aperture. Connected above the input aperture is a small 'lipstick' camera that picks off approx 1% of the input light. The video from this camera is fed to a monitor and used for target acquisition. This version of the MR-304 is uncooled, since the detected wavelengths range from the shortwave to the visible spectrum. Therefore, self emission is negligible in the operating spectral range.

3.2   Smoky SAM Test

The Smoky SAM is a scaled down model version of an operational surface to air missile. It is propelled with combustion material similar to full scale missiles, so its

Figure 16. Picture of the Smoky SAM during combustion. The Smoky SAM was held in this fixed position for the duration of the test. The observed plume was approximately 2 - 3 ft long and burned for 5 seconds.

emissive spectrum is close to that of commonly used SAMs. For the duration of the test, the Smoky SAM was held in a fixed position while the missile motor burned to completion, as shown in Figure 16. The emissive plume exiting the rear of the Smoky SAM was approximately $2 - 3$ ft in length. During data collection, the FOV of the telescope was entirely filled with the hot plume against a smoky background. Therefore, the backdrop of trees and cars were not in the FOV. The motor burn was fairly short, lasting only five seconds.

The range between the MR-304 and the Smoky SAM was measured, using Google Earth, to be 409 meters. Since Google Earth uses GPS oriented imagery, it was assumed that the provided range measurements were accurate to within 5 %. Therefore, the Smoky SAM truth measurement of range was taken to be accurate within 20 meters. A more precise measure of range was not achievable, due to safety restrictions near a highly flammable source.

Meteorological data was recorded with a hand held Kestrel 9500 instrument. The

31

Table 3. Smoky SAM instrument settings and meteorological data taken immediately after observation. Here resolution refers to spectral resolution in wavenumbers.

MR-304	Telescope	Field Stop	Gain	Resolution	Frame Rate
	4.9 mrad	6.4 mm	32	$4\,\mathrm{cm}^{-1}$	$\sim 40\,\mathrm{Hz}$

Weather	Temperature		Pressure	Dew Point
	$26.0^o\,\mathrm{C}$		$991.8\,\mathrm{hPa}$	$17.04^o\,\mathrm{C}$

Geometry	Sensor Altitude	Sensor Zenith Angle
	$244\,\mathrm{m}$	89°

Kestrel provided measurements of temperature, pressure, and relative humidity. The relative humidity was then converted into dew point. The amount of water vapor in the air is important to know, because it displaces oxygen by a small but measurable amount. This meteorological data is presented in Table 3.

The number density of oxygen was computed and found to be $4.99 \times 10^{24}\,\mathrm{m}^{-3}$. A more detailed discussion of the density calculation is presented in reference [7]. To compare with the modeled absorption, the density of oxygen used by LBLRTM was referenced from the resulting Tape 6 file and found to be $5.07 \times 10^{24}\,\mathrm{m}^{-3}$. A Tape 6 file is a text file created during an LBLRTM computation that specifies the complete set of atmospheric parameters used to model transmission. The ratio of these two densities provided the atmospheric range correction parameter, $C_R = 0.985$.

Given the compact size of the Smoky SAM, the telescope with the largest available aperture was chosen to maximize signal. There were five Smoky SAMs fired throughout the course of the day, so a variety of instrument settings could be tested. The settings that yielded the best spectrum are shown in Table 3.

Figure 17 shows the observed spectral response from the Smoky SAM, averaged over 180 frames without apodization. The emission spectra of the Smoky SAM appears to be radiating continuously over a broad spectral band, with the obvious exception of the two large spikes near $13,000\,\mathrm{cm}^{-1}$. These two spikes are doublet emission lines from heated potassium; it is a common trace contaminant in solid
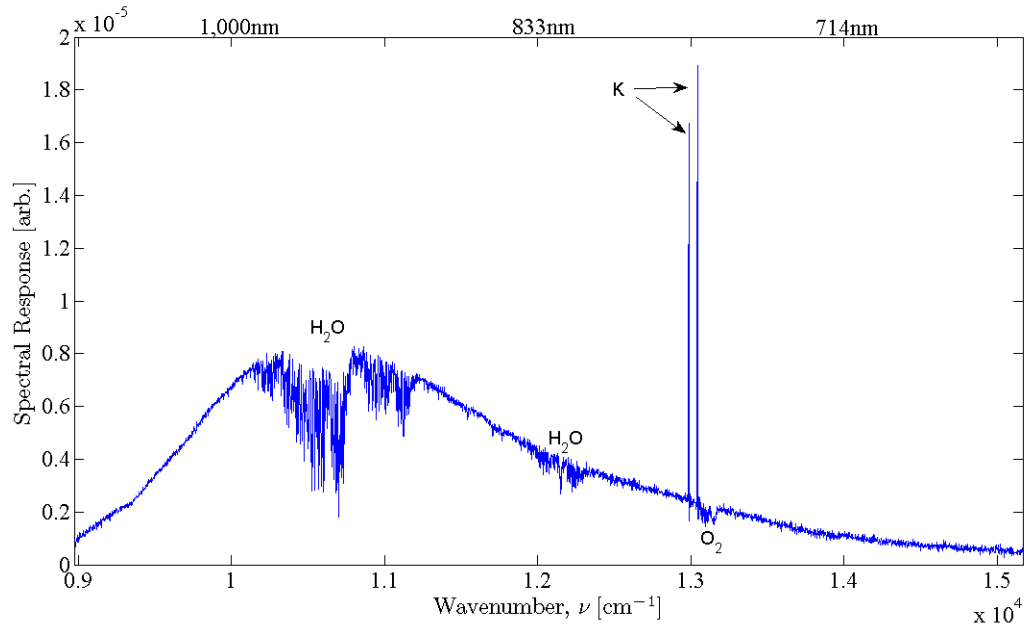
Figure 17. **MR-304 spectral response of the Smoky SAM emission plume, averaged over 180 frames of steady signal. The spectral resolution was set to $4\,\mathrm{cm}^{-1}$. The large potassium emission lines are labeled with its chemical symbol. The prominent water absorption features are labeled, as well as the NIR O_2 absorption band. The Vis O_2 band is not apparent in this plot.**

rocket fuel. The absorption features in the spectrum correspond to absorption by atmospheric constituents. Notably, there are strong water absorption bands centered at $10,800\,\mathrm{cm}^{-1}$ and $12,100\,\mathrm{cm}^{-1}$.

A closer look at the NIR O_2 band is shown in Figure 18. Notice that the potassium lines reside directly in the P-branch of this band. At 409 meters there is a noticeable amount of absorption in the R-branch (green on Figure 18). The baseline, interpolated from out-of-band data, is presented as the dashed red line.

Figure 19 is a closeup of the Vis O_2 band; the R-branch is also shown in green. At this distance there is basically no measurable absorption in the Vis band with the present noise. The lack of apparent absorption is primarily due to the weaker line strength transitions of the Vis band, and the decrease in radiated signal from the emission plume as compared to the NIR O_2 band.
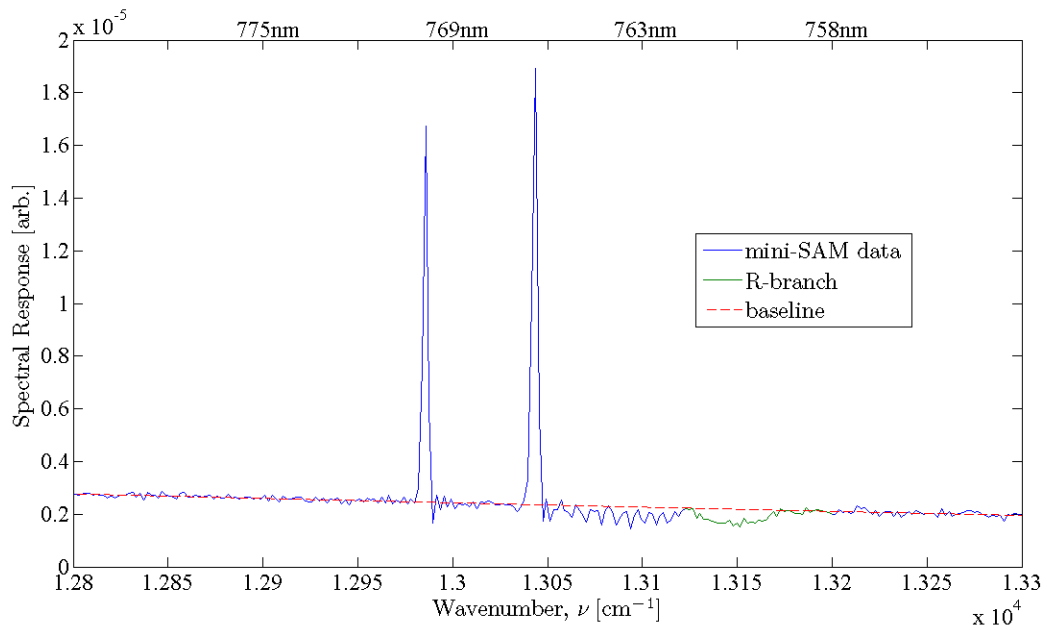
Figure 18. A closeup of the NIR O_2 absorption band for the Smoky SAM test. The R-branch is shown in green, while the baseline is shown as the dashed red line. Notice that the potassium lines reside directly in the P-branch.
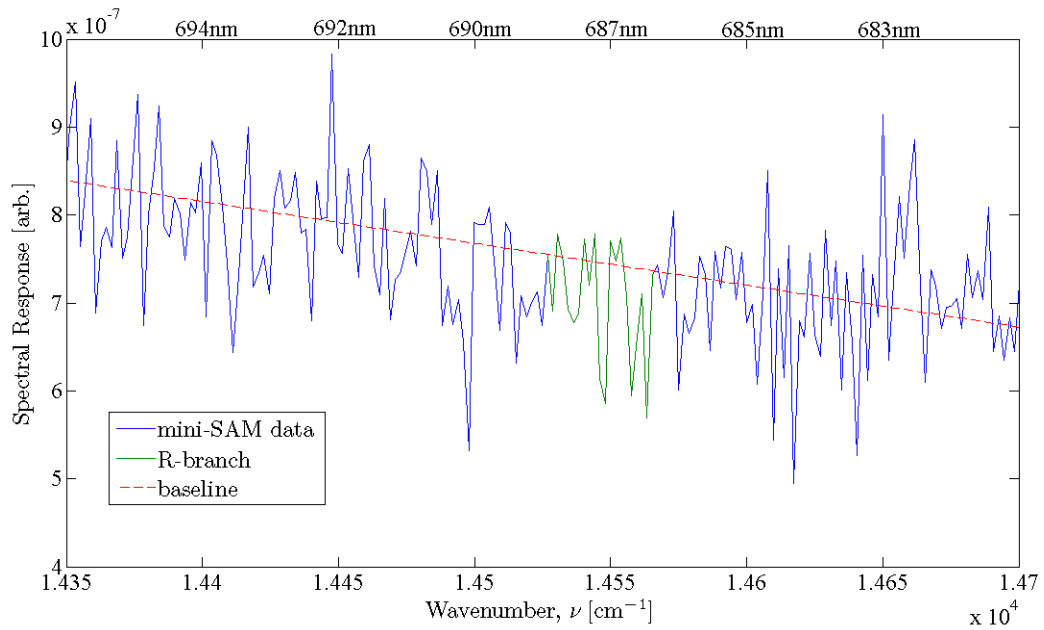
Figure 19. A closeup of the Vis O_2 absorption band for the Smoky SAM test. The R-branch is shown in green, while the baseline is shown as the dashed red line. At 409 meters there is no noticeable absorption in this band.

34

Table 4. Static solid rocket motor test (SRT) instrument settings and meteorological data taken five minutes before observation. The sensor was placed at a higher altitude than the rocket. Therefore, the zenith look angle is greater than 90 degrees.

MR-304	Telescope	Field Stop	Gain	Resolution	Frame Rate
	76 mrad	6.4 mm	1	$1\,\mathrm{cm}^{-1}$	$\sim 10\,\mathrm{Hz}$
Weather	Temperature		Pressure		Dew Point
	$28.8^o\,\mathrm{C}$		$844.9\,\mathrm{hPa}$		$2.82^o\,\mathrm{C}$
Geometry	Sensor Altitude		Sensor Zenith Angle		
	$1.50\,\mathrm{km}$		96.7^o		

3.3 Static Solid Rocket Motor Test

Solid rocket fuel is a commonly used propellant that provides a large amount of thrust for rockets and missiles during liftoff. In fact, the NASA Space Shuttles use solid rocket boosters to provide the majority of their liftoff thrust. A solid rocket motor test was observed in 2010 at a testing facility in the Western United States. The static rocket test (SRT) involved a full scale solid rocket motor that was fixed in a static position for the duration of the combustion; the burn lasted for approximately 35 seconds.

Figure 20 shows a compilation of pictures taken during the SRT. The top row of pictures show the sensor arrangement, and the bottom row shows the SRT during combustion. The MR-304 was positioned looking slightly downward at the SRT from a higher altitude. Direct line-of-sight range to the SRT from the MR-304 was calculated, using Google Earth, to be $900 \pm 45\,\mathrm{m}$. The Kestrel weather instrument was again used to measure weather data and was recorded 5 minutes prior to the SRT. Table 4 displays the instrument settings, weather data, and geometry taken during the SRT. Since the SRT was significantly brighter and burned for longer than the Smoky SAM, the MR-304 was set to a finer spectral resolution of $1\,\mathrm{cm}^{-1}$.

Using the weather data in Table 4, the number density of O_2 at the test site was calculated to be $3.71 \times 10^{24}\,\mathrm{m}^{-3}$. The LBLRTM number density at this altitude, ref-

35

Figure 20. Pictures of the static solid rocket motor test. Top row: pictures of the instrument suite setup in the AFIT remote sensing trailer. Bottom row: pictures of the solid rocket motor and emission plume during ignition.

erenced from the Tape 6 file, was recorded as $4.50 \times 10^{24}\,\mathrm{m}^{-3}$. The atmospheric range correction parameter was then calculated as $C_R = 0.824$. A likely explanation for the large deviation of C_R from unity is that the test was held during a hot summer's day, while the 1976 U.S. Standard Atmosphere presents concentrations closer to a seasonal average. This is consistent with an ideal gas approximation, where concentration is inversely proportional to temperature with constant pressure.

The spectrum of the solid rocket motor plume is shown in Figure 21; 200 spectral frames were averaged together to produce this low noise spectrum. Several emission lines are present in this spectrum and are due to alkali metal contaminants in the
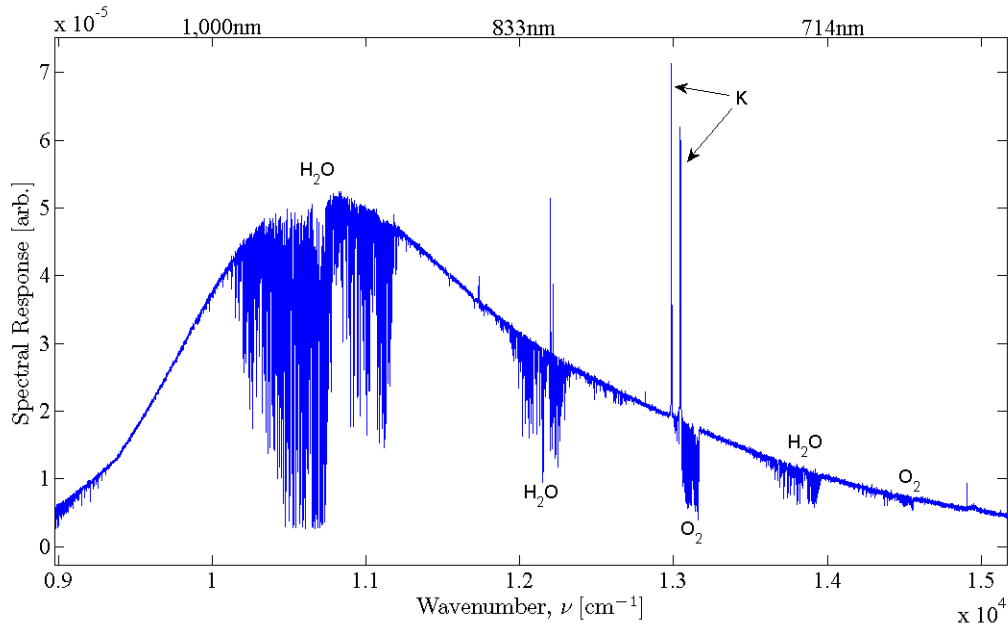
Figure 21. MR-304 spectral response of the static solid rocket motor emission plume, averaged over 200 frames. The spectral resolution was set to $1\,\mathrm{cm}^{-1}$. The large potassium emission lines are labeled with its chemical symbol. The prominent water absorption features are labeled, as well as the NIR & Vis O_2 absorption bands.

solid rocket rocket fuel. Figure 22 shows again the presence of potassium emission lines in the NIR O_2 P-branch. At this resolution, each doublet absorption line in the P-branch is resolved. This figure shows that the out-of-band regions have low noise levels compared to the in-band absorption.

Figure 23 displays the Vis O_2 absorption band observed from the SRT. At a 900 meter range, absorption in the Vis O_2 band is definitely noticeable. However, comparing Figure 23 to Figure 22 shows that the Vis O_2 band is much noisier than the NIR O_2 band. For both figures the interpolated baseline is shown as the dashed red line. Figure 23 also shows absorption due to water vapor overlapping with the Vis O_2 P-branch, as modeled in LBLRTM.

37
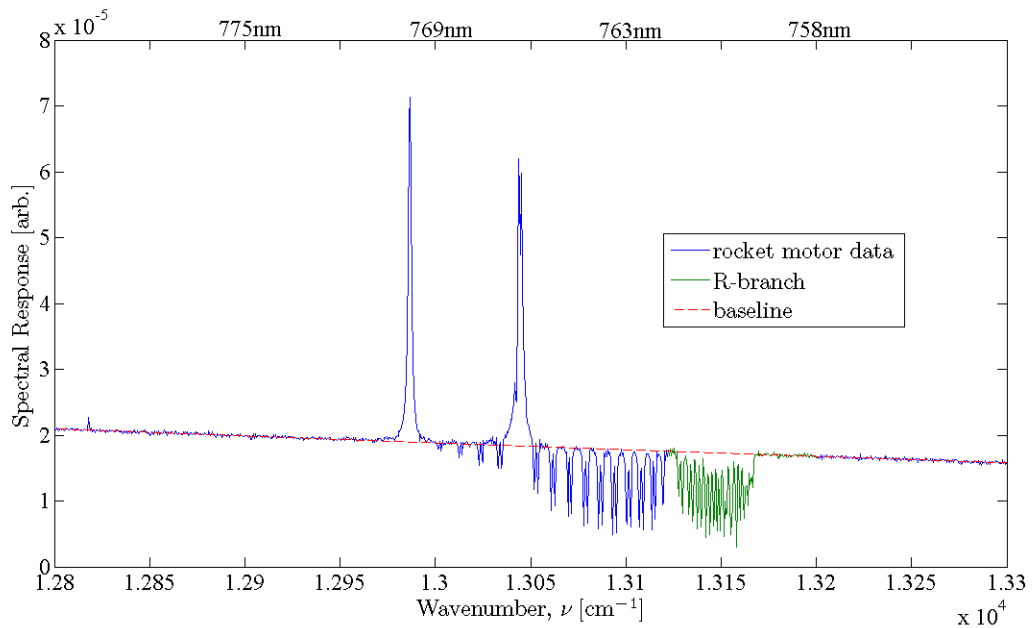
Figure 22. A closeup of the NIR O_2 absorption band for the static solid rocket motor test. The R-branch is shown in green, while the baseline is shown as the dashed red line. The emission lines are due to alkali metal contaminants in the solid rocket fuel.
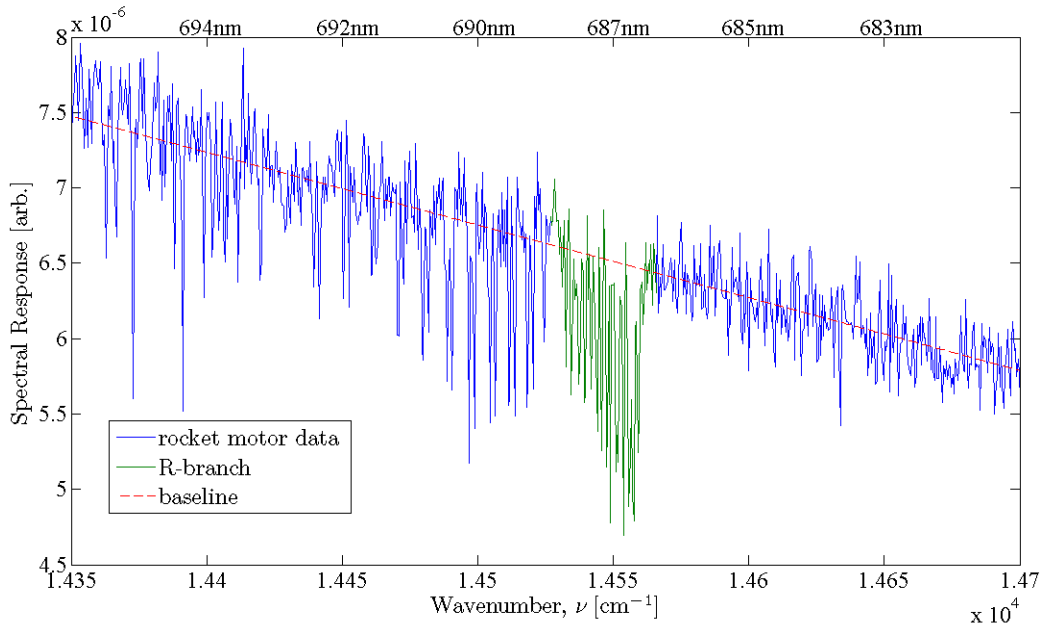
Figure 23. A closeup of the Vis O_2 absorption band for the static solid rocket motor test. The R-branch is shown in green, while the baseline is shown as the dashed red line.

38

3.4 SpaceX: Falcon 9 Rocket Launch Observation

For the past three decades, manned U.S. space flight has been launched with the iconic NASA Space Shuttles. During the calendar year 2011, all three remaining Space Shuttles are scheduled to fly their final mission and will be subsequently retired. In their place, NASA has awarded a multi-billion dollar contract to SpaceX, a privately owned aerospace corporation, to design their own launch vehicle that may one day carry astronauts to the International Space Station. On December 8th, 2010, SpaceX launched their Falcon 9 rocket into a low Earth orbit for an operational milestone test of their "Dragon" capsule. After a few quick orbits, the Dragon used parachutes to return safely to the Earth's surface.

The Falcon 9's first stage consists of nine "Merlin" engines based upon the earlier design of the Saturn V and Saturn I rockets used in the NASA Apollo program. These engines use rocket grade kerosene and liquid oxygen for combustion. Kerosene is a common fuel used to provide thrust for numerous aircraft and rocket motors. Therefore, the spectral signature of the combustion products is of interest for applications of national security and defense.

Observation of the Falcon 9 launch was performed at the Innovative Science and Technology Experimentation Facility (ISTEF), located on Merritt Island, Florida. ISTEF is managed by the U.S. Navy; however, they are frequently tasked to provide electro-optical and radar systems support for NASA and other government agencies. This is because of their close proximity to the Kennedy Space Center for observing rocket launches. Figure 24 shows a satellite view of the Kennedy Space Center and Merritt Island area. The Falcon 9 launch pad, ISTEF, and the nearest weather station are labeled for reference. The distance between ISTEF and the Falcon 9 launch pad was calculated from GPS coordinates to be 13.05 km.

Three AFIT sensors were mounted on a tracking platform that followed the tra-

39
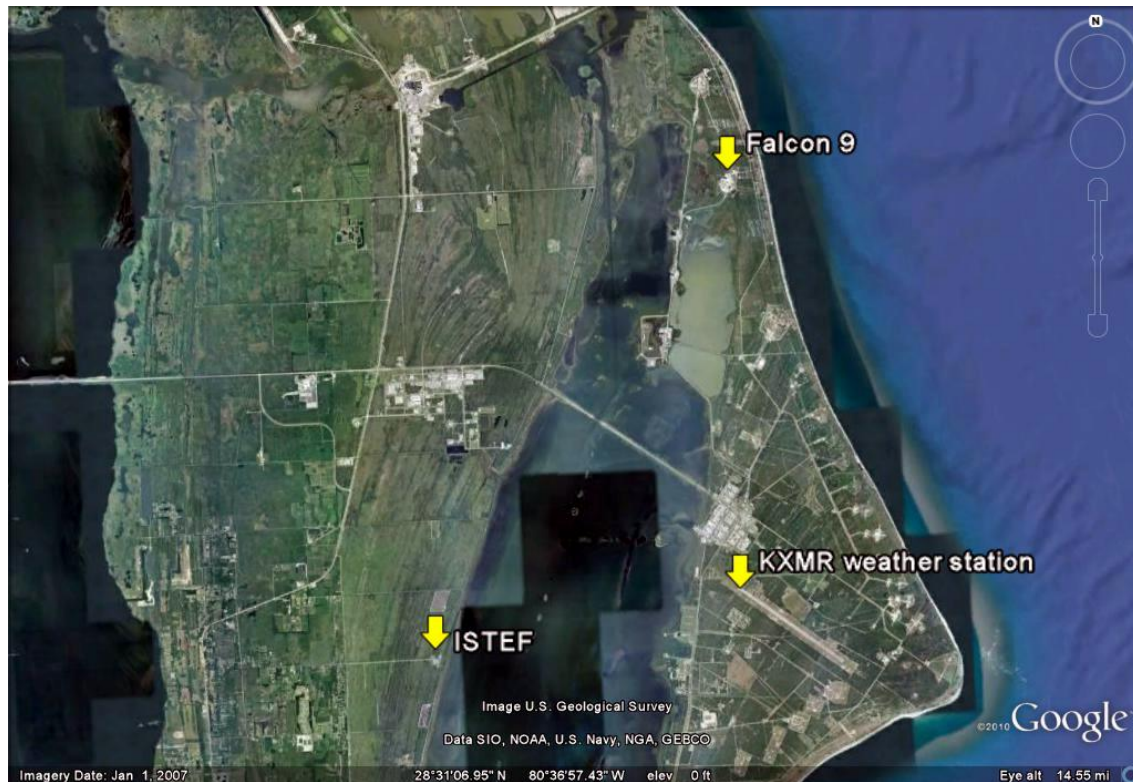
Figure 24. Satellite view of the Kennedy Space Center and Merritt Island area. The Falcon 9 launch pad, ISTEF tracking facility, and the nearest weather station are annotated. Distance between ISTEF and launch pad was calculated to be 13.05 km.

jectory of the Falcon 9 through its launch. Figure 25 shows several pictures of the tracking mount with attached AFIT sensors. The lower right picture shows the instrument control setup located in the AFIT deployable trailer, parked next to the tracking mount. The three mounted instruments include the NIR/Vis MR-304 used in this research, a MWIR MR-304, and a Phantom high-speed camera.

The ISTEF mount, referred to as the "Black Mace", is capable of following a pre-calculated trajectory. For the Falcon 9 launch, an estimated trajectory was loaded into the Black Mace, while a mount operator applied small manual corrections during launch. The video from the MR-304 acquisition camera was piped into the mount operator's control room, such that the rocket plume was centered in the MR-304 FOV. Controls applied to the Black Mace, such as azimuth and elevation, were saved

Figure 25. Pictures of the Black Mace mount setup located at ISTEF. Bottom right, picture of the AFIT instrument control setup.

into a text file and used in the post-processing of the observed data.

The MR-304 instrument settings and recorded meteorology data are displayed in Table 5. Since the observed radiance from the Falcon 9 decreased with flight time, the auto-gain setting was used for the MR-304. This was done to maximize the duration of usable signal. While there may be a question of temporal response to rapidly changing scenes, the auto-gain setting appeared to work flawlessly.

The weather data was taken from the nearest weather station, designated KXMR, and recorded ten minutes after liftoff. Using this weather data, the number density of oxygen near sea level was calculated to be $5.36 \times 10^{24}\,\mathrm{m}^{-3}$. The referenced number density in the LBLRTM Tape 6 file was $5.28 \times 10^{24}\,\mathrm{m}^{-3}$. Finally, the atmospheric range correction parameter was found to be $C_R = 1.015$.

www.manaraa.com

Table 5. **Falcon 9 observation settings and meteorology data taken 10 minutes after launch.**

MR-304	Telescope	Field Stop	Gain	Resolution	Frame Rate
	4.9 mrad	6.4 mm	*auto*	4 cm^{-1}	$\sim 40\,\text{Hz}$
Weather	Temperature		Pressure		Dew Point
	12.5^o C		1020.7 hPa		2.44^o C
Geometry	Sensor Altitude		Sensor Zenith Angle		
	$\sim 3\,\text{m}$		*variable*		

Several pictures of the Falcon 9 before and during liftoff are displayed in Figure 26. The middle right photo in this figure is a frame from the MR-304's acquisition camera, recorded 40 seconds into the flight. This shows that the emissive rocket plume fills approximately 1/8 the FOV, with a blue sky background. As discussed in the previous chapter, the background radiances from the blue sky are assumed to be negligible. For verification, the rocket trajectory was rerun three minutes after the Falcon 9 launch, gathering just blue sky background. While direct comparisons between sky background and the Falcon 9 are complicated by using the auto-gain function, the background radiances were several orders of magnitude less than the Falcon 9 plume at 13 km.

Figure 27 shows the SNR values per frame of the Falcon 9 NIR and Vis spectra during flight. The SNR was calculated from the out-of-band frequencies given in Table 1. The MR-304 was triggered to begin recording data three seconds before rocket ignition. For the first 20 seconds of flight the Falcon 9 was hidden behind a canopy of trees. The rocket fully cleared the trees 25 seconds after ignition. This was followed by 70 seconds of successful tracking and observation until the Black Mace lost track for 20 seconds. The Falcon 9 was then reacquired in the MR-304 at 120 seconds into flight. After this point, Figure 27 shows that the NIR and Vis signal rapidly diminished to noise. Notice that the SNR in the NIR O_2 band is about four times that of the Vis O_2 band for the duration of usable signal.

42
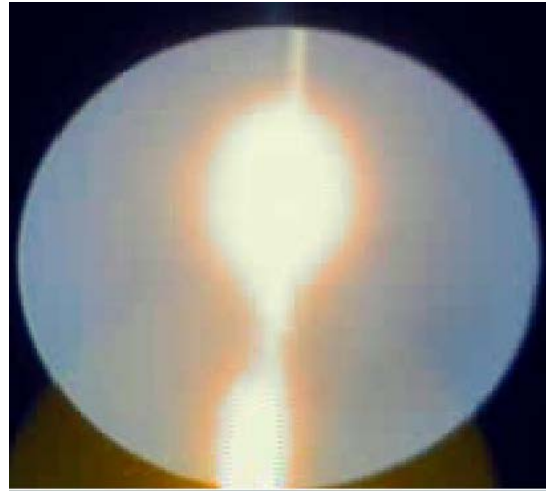
Figure 26. Pictures of the Falcon 9 rocket before and during launch. Top and middle left, credit to SpaceX. Middle right, picture of rocket 40 sec. into launch as observed from the MR-304 acquisition camera. Bottom, credit to Space Flight Now.
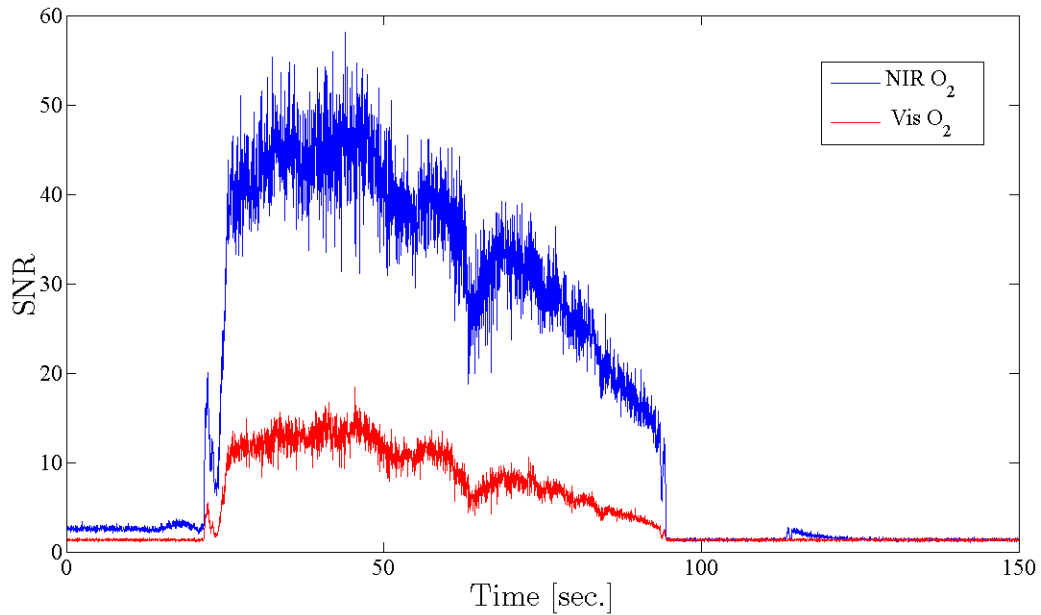
Figure 27. MR-304 measured SNR values per frame from the Falcon 9 rocket. SNR values were spectrally calculated from the out-of-band frequencies presented in Table 1. The 20 second dropout starting at 95 seconds into flight was due to the mount temporarily losing track of the rocket.

The mean spectrum, presented in Figure 28, was averaged over the $2,000$ frames recorded during the 70 seconds of Falcon 9 observation data. Interestingly, there appear to be no emission lines from alkali metal contaminants. The spectrum from the kerosene motor looks very similar to that of a hot blackbody radiator; the absorption features due to atmospheric species along the observation path. The NIR and Vis O_2 bands are magnified in Figure 28 for comparison. Note that the R-branch in the NIR O_2 band is nearly saturated, while the Vis O_2 R-branch is not.

3.5   Summary

Three rocket and missile tests were successfully observed during the experimental phase of this research. Appropriate instrument settings and optics were used, providing quality data with sufficiently high signal levels and no saturated detectors. Static

44
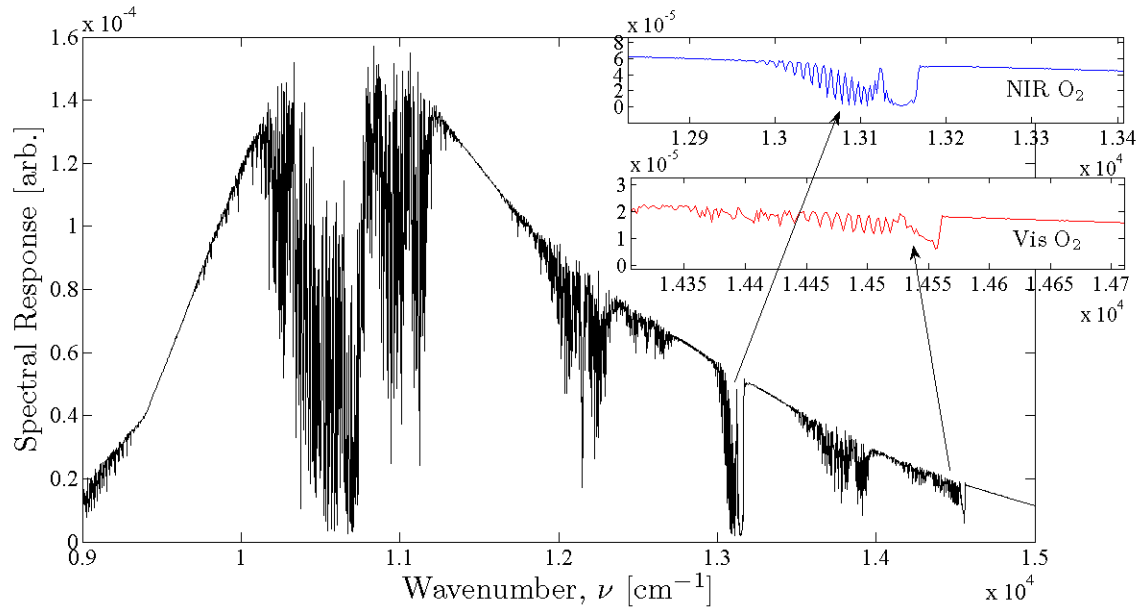
Figure 28. The spectral response measured by the MR-304 during the 70 sec. of Falcon 9 observation. This spectrum was averaged over 2,000 frames. The NIR (top) and Vis (bottom) O_2 bands are magnified for comparison.

solid fuel motors were observed at 400 and 900 meters, and a kerosene/liquid oxygen powered rocket was tracked for 70 seconds during liftoff at an initial range of 13 km.

IV. Results and Analysis

With measured spectra from the three rocket motors discussed in the previous chapter, band averaged absorption was calculated, and range estimated from referencing LBLRTM modeled transmission. Since the Smoky SAM and SRT were held in a fixed position, their temporal behavior was not examined in detail. The spectral frames measured during ignition were averaged together in order to generate one low-noise spectrum, and used to calculate a single range estimate. In contrast, dynamic range estimates of the Falcon 9 rocket are crucial for validating the concept of MPR for moving targets. Therefore, estimates of range versus flight time are presented for the Falcon 9 rocket; while they are not presented for the Smoky SAM and SRT.

4.1 Static Range Estimates

The MPR range estimates from the Smoky SAM and SRT are presented in Table 6. The third column, denoted as Range Est., displays the raw range estimates without an applied atmospheric correction for O_2 concentration. The range estimates with the included atmospheric correction are shown in column 5. Range values calculated from GPS coordinates are given in column 6, labeled Truth. Percent error is shown in the last column and is simply the corrected range estimates divided by the Truth values.

Results in Table 6 corroborate previous research for the NIR O_2 band, showing that it can be used to passively estimate range to an emissive target with an error less than 3% for ranges between 400 and $900\,\mathrm{m}$. The Vis O_2 band, however, does not yield accurate range estimates for ranges less than $900\,\mathrm{m}$. This is not a surprising result, because the Vis O_2 band is approximately an order of magnitude weaker in absorption than the NIR O_2 band. Consequently, the hypothesized trade-off, where

Table 6. Calculated range estimates for both static motor tests. The column labeled "Range w/C_R" displays the product of the raw range estimates multiplied by C_R, to correct for current atmospheric conditions.

Test Name	O$_2$ Band	Range Est.	C_R	Range w/C_R	Truth	% Error
Smoky SAM	NIR	406 m	0.985	$40\overline{0} \pm 202$ m	405 m	2.2 %
	Vis	726 m		$715 \pm 1,935$ m		76.5 %
SRT	NIR	1060 m	0.824	876 ± 108 m	$9\overline{00}$ m	2.7 %
	Vis	925 m		763 ± 519 m		15.2 %

the Vis band yields more accurate range estimates, may occur at ranges greater than 900 m.

A graphical representation of the Smoky SAM results for the NIR O$_2$ band is shown in Figure 29. The observable metric, $\bar{A}$, is shown as the vertical axis, while range is given as the horizontal axis. The relationship between $\bar{A}$ and range, as generated by LBLRTM, is plotted as the blue line. Measured absorption is displayed as the horizontal black line, estimated range is the vertical black line, and the true range is annotated with a green star. The dashed lines represent the uncertainty in $\bar{A}$ ($\sigma_{\bar{A}}$) and how it translates into range uncertainty (σ_R) via the referenced absorption curve.

Uncertainty is calculated with the assumption that noise in the out-of-band data has a standard deviation based upon a normal distribution. It is assumed that this standard deviation also applies to the interpolated baseline, resulting in a 68 % confidence interval for $\bar{A}$. This confidence interval is displayed as the horizontal dashed lines in Figure 29. Since the absorption curve is nonlinear, a symmetric statistical distribution of $\bar{A}$ values leads to an asymmetric distribution of range values. The asymmetry for range uncertainty is apparent in Figure 29 by comparing the vertical dashed lines to the corrected range estimate (solid vertical line). If given a distribution of range estimates, a median calculation may be more accurate than an arithmetic mean for estimating the true range.

Figure 30 is similar to the previous figure, except it displays the Smoky SAM results for the Vis O_2 band. The Vis band significantly overestimates range by 77%. The lower dashed lines of $\sigma_{\bar{A}}$ are not shown, because they extend to negative absorption values. Negative absorption is clearly unphysical. The large uncertainty in this range estimate is referenced back to the Smoky SAM visible spectrum, Figure 19, where absorption in the Vis band was unnoticeable at $405\,\mathrm{m}$.

SRT results are visualized for the NIR band in Figure 31, and Figure 32 for the Vis band. The NIR O_2 band yields an accurate range estimate with significantly less uncertainty than the Smoky SAM test, mainly due to the longer observation time. The Vis O_2 band for the SRT was much more accurate than in the Smoky SAM test, but only to within 15% of the true range. The uncertainty in the Vis band range estimate is greater than the NIR band estimate for two principle reasons. There is less absorption in the Vis band and there is less spectral radiance in the visible spectrum compared to the NIR spectrum for a black body radiator at a temperature less than approx $5,000^o\,\mathrm{C}$. The FTS response is also lower at higher frequencies.

In conclusion, these results show that for ranges less than $900\,\mathrm{m}$ the NIR O_2 band provided more accurate range estimates with less uncertainty than the Vis O_2 band. This is expected to be true for increasing ranges until saturation effects become noticeable in the NIR band. It is somewhat surprising that this technique produced results accurate to 2.2% for the Smoky SAM tests, given its short duration and dim signal. The Smoky SAM results show that MPR can be used to estimate ranges for a variety of smaller emissive targets, not just full-scale rocket motors. It also highlights that a spectral resolution coarser than 1 or $2\,\mathrm{cm}^{-1}$ can be used to achieve equally accurate range estimates.

Figure 29. NIR O$_2$ range estimate for Smoky SAM. The blue curve was generated by LBLRTM. The solid black lines show the measured absorption translated into a range estimate. The dashed black lines depict a 68 % confidence interval.
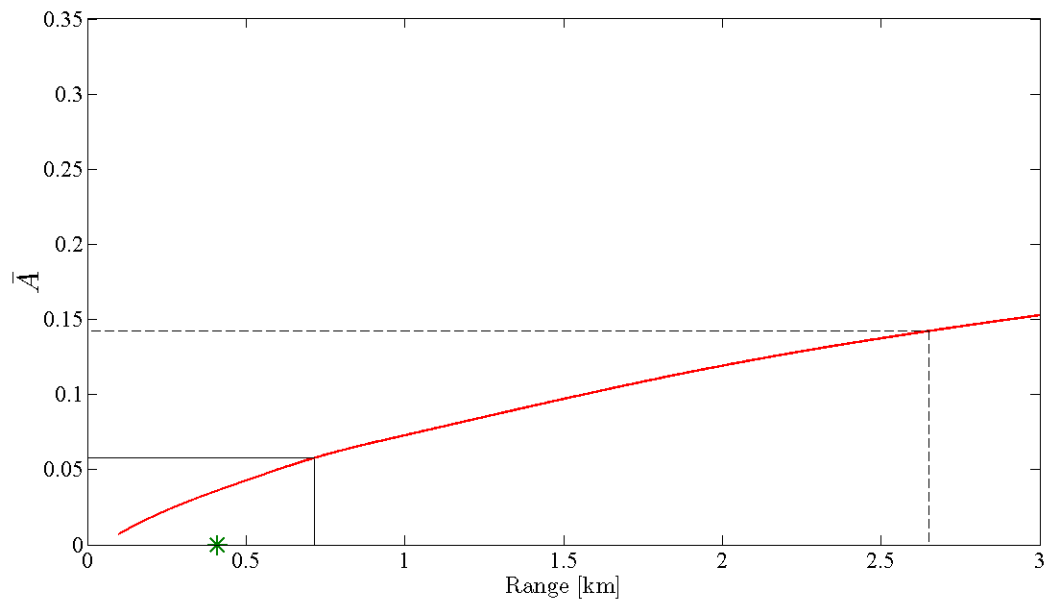
Figure 30. Vis O$_2$ range estimate for Smoky SAM. The red curve was generated by LBLRTM. The solid black lines show the measured absorption translated into a range estimate. The dashed black lines depict the upper limit of a 68 % confidence interval. The lower limit is not shown, because it extends into negative absorption values.

49
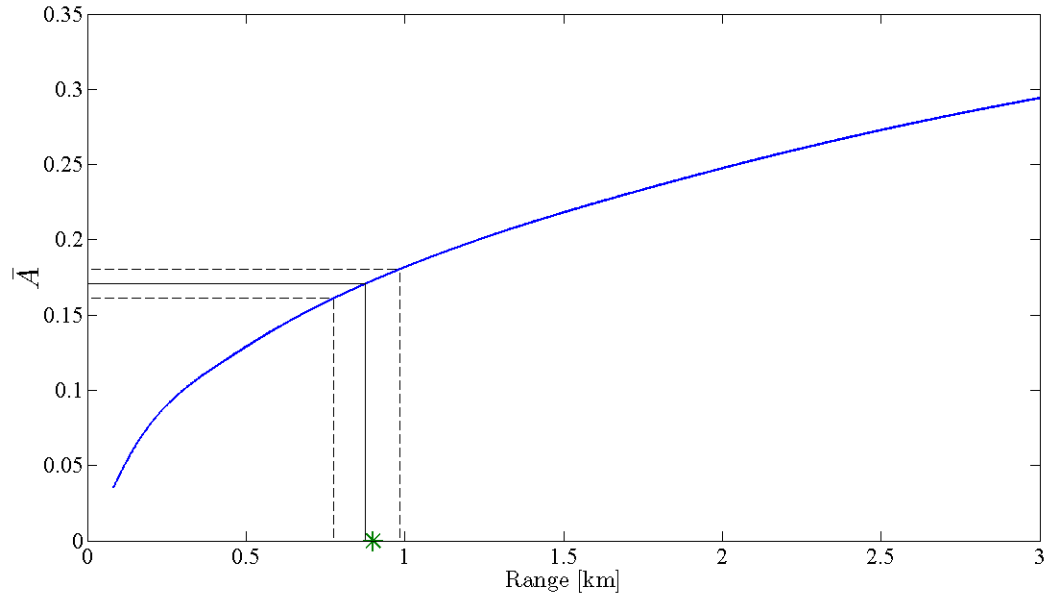
Figure 31. NIR O_2 range estimate for the SRT. The blue curve was generated by LBLRTM. The solid black lines show the measured absorption translated into a range estimate. The dashed black lines depict a 68 % confidence interval.
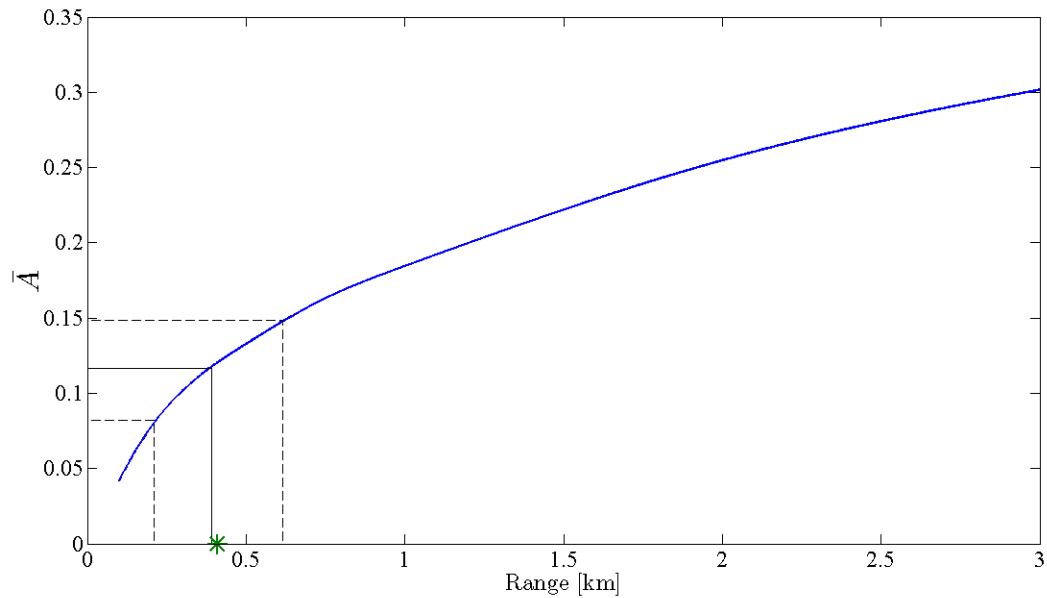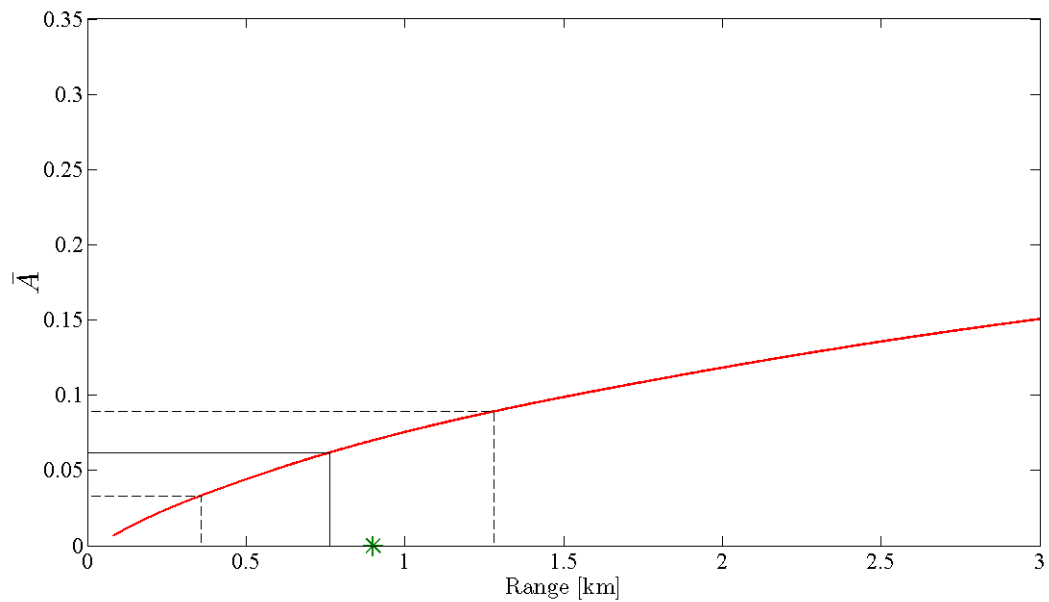

Figure 32. Vis O_2 range estimate for the SRT. The blue curve was generated by LBLRTM. The solid black lines show the measured absorption translated into a range estimate. The dashed black lines depict a 68 % confidence interval.

4.2 Falcon 9 Rocket Launch Results

As previously shown in Figure 27, the SNRs per frame for the Falcon 9 observation peaked around 50 for the NIR band and 15 for the Vis band. For Falcon 9 analysis, a running average was used to decrease noise in the spectrum and increase SNR values for the out-of-band oxygen frequencies. The downside to using a running average is that the temporal details get smeared across the number of frames used to calculate the arithmetic mean. The "bucket" size for the running average included 65 frames per average. The time-stamp of the center frame was associated to the averaged value, such that the time axis from launch remained unchanged. Given a frame rate of 40 Hz, temporal fidelity was maintained for time intervals of approximately 1.5 seconds.

4.2.1 In-Flight Range Estimates.

The top plot in Figure 33 shows the measured values of $\bar{A}$ during the Falcon 9 launch. The blue line represents the NIR O_2 band and the red line represents the Vis O_2 band. For the first 20 seconds after ignition the MR-304 was staring at dense vegetation. The high $\bar{A}$ values in the NIR band during this time are due to observing vegetation reflectance spectra. Once the Falcon 9 cleared the tree canopy, absorption from the rocket plume was measured for 70 straight seconds. Notice that there was a slight but steady decline in $\bar{A}$ during ascent. The Falcon 9 was not getting closer to the observation sight, but was gaining altitude and traveling through thinning air. Therefore, the decline in $\bar{A}$ during flight was due to less oxygen in the observing path as the Falcon 9 left the thick sea level atmosphere.

The top-middle plot in Figure 33 displays the uncertainty in absorption, $\sigma_{\bar{A}}$, during flight. The bottom-middle plot shows the sensor zenith angle (ϕ) as measured by the control system of the ISTEF tracking mount. Finally, the bottom plot is of the SNR values measured from out-of-band frequencies, similar to Figure 27. These plots show

51

that the Vis band has roughly half the SNR and slightly more absorption uncertainty than the NIR band during the 70 second observation window. It may be tempting to conclude that the NIR O_2 band clearly outperformed the Vis O_2 band; however, this can only be determined by analyzing the resulting range estimates.

The range estimates from both O_2 bands during flight are presented in the top plot of Figure 34. Once again, the blue curve relates to the NIR band and the red curve to the Vis band. The black curve represents the true range from the tracking mount to the Falcon 9. During launch, radar sensors operated by the Cape Canaveral Air Force Base were able to calculate what is commonly referred to as the best estimate trajectory (BET) of the Falcon 9 rocket. The BET was provided as x,y,z coordinate vectors from the center of the Earth. This coordinate system is known as Earth-Centered, Earth-Fixed (ECEF) coordinates. By converting the latitude, longitude, and altitude of the sensor to ECEF coordinates, the true range was calculated simply with vector algebra.

Analysis of the top plot shows that the Vis O_2 range estimates closely overlap with the truth range for the first 30 seconds of tracked flight. In fact, the Vis range estimates are accurate with an error less than 8 % for this time period. Around 70 seconds into flight the Vis range estimates began to degrade significantly until the mount lost track 95 seconds after ignition. The spurious range estimates 90 seconds into flight correspond to measured values of $\bar{A}$ that fall outside of the referenced lookup table shown in Figure 13. This demonstrates that care must be taken when interpolating outside the constructed parameters of the system. There are several methods available for mathematical interpolation. A few examples are nearest neighbor, linear, and cubic spline. A linear interpolation was chosen in this range calculation in order to minimize the effects of interpolating outside the given boundaries provided by LBLRTM.
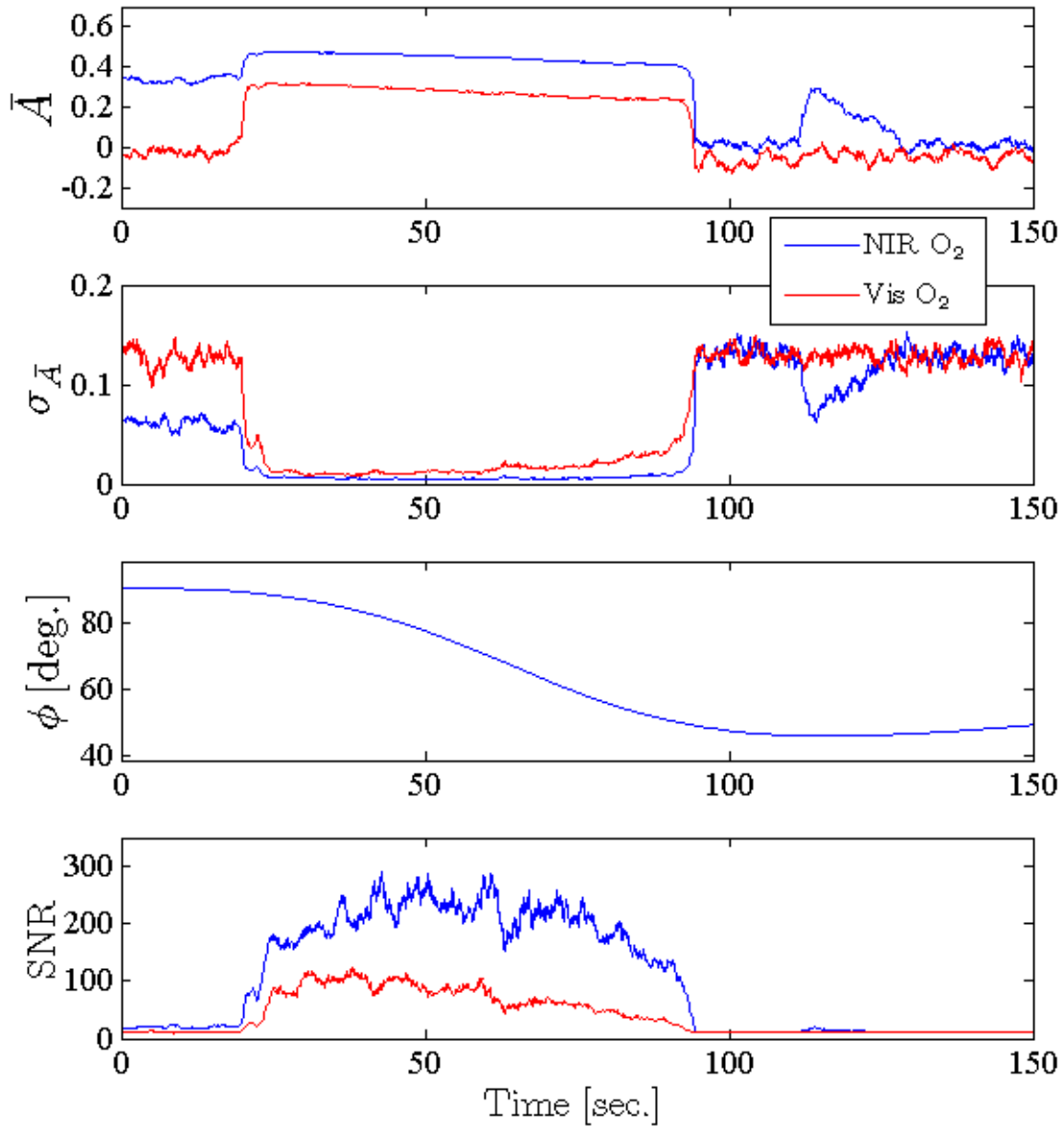
Figure 33. Top: Measured $\bar{A}$ values for each O_2 band of the Falcon 9 rocket during launch. Top-Middle: Uncertainties in $\bar{A}$ for each O_2 band. Bottom-Middle: Measured zenith angles of the sensor during launch. Bottom: SNR values measured from out-of-band frequencies during flight. Plots of absorption and SNR used a 50 frame running average to reduce noise in the $\bar{A}$ measurements.

53

Figure 34. Top: Range estimates for each O_2 band of the Falcon 9 rocket during launch using a 1976 U.S. standard atmospheric profile. The black line represents the true range between sensor and Falcon 9 after ignition. Top-Middle: Uncertainties in range estimates for each O_2 band. The spurious lines after approx 70 seconds arise from interpolated $\bar{A}$ values outside of the given lookup table. Bottom-Middle: The absolute value of the difference between the true range and the estimated range, also referred to as the residual error. Bottom: Approximated altitude of the Falcon 9 during launch, calculated from the truth range and the measured zenith angle.

54

The NIR band overestimated range by 2 km at first rocket acquisition, then steadily worsened for the next 50 seconds. Around 80 seconds into flight the NIR band stopped yielding range values, because the measured $\bar{A}$ values led to interpolation outside the given lookup table. Comparing this effect to the Vis band, the NIR band stopped giving potentially useful range estimates approximately 10 seconds before the Vis band did.

The top-middle plot in Figure 34 shows the uncertainty, σ_R, in the range estimates for both O_2 bands. For the first 50 seconds of tracked rocket flight, both O_2 bands had similar σ_R values. This is an interesting result given the $2 - 3$ km error in the NIR O_2 band compared to the Vis band. A possible cause of this few kilometer shift may be an unnoticeable bias in the $\bar{A}$ measurement that is greatly enhanced by referencing an absorption curve near saturation.

The magnitude of the difference between the true range and estimated range is displayed in the the bottom-middle plot of Figure 34. This metric is also known as residual error and can be compared to the σ_R values. Note that the residual error in the Vis band is discernibly lower than its uncertainty. To the contrary, the NIR band has slightly greater residual error than its uncertainty, which again points to a systematic NIR band error. However, it is somewhat surprising that the NIR O_2 band produced range estimates this accurate given the amount of in-band saturation apparent in the mean spectrum shown in Figure 28.

In an effort to characterize the bias in the NIR range estimates, the entire ranging calculation was repeated using a tropical atmospheric profile instead of a 1976 U.S. Standard Atmosphere profile, as shown in Figure 35. Lookup tables of $\bar{A}$ versus range and zenith angle were recalculated for a tropical model using the script shown in Appendix B. The saved lookup tables were then passed to the range computation algorithm shown in Appendix C. In the end, the range results using a tropical
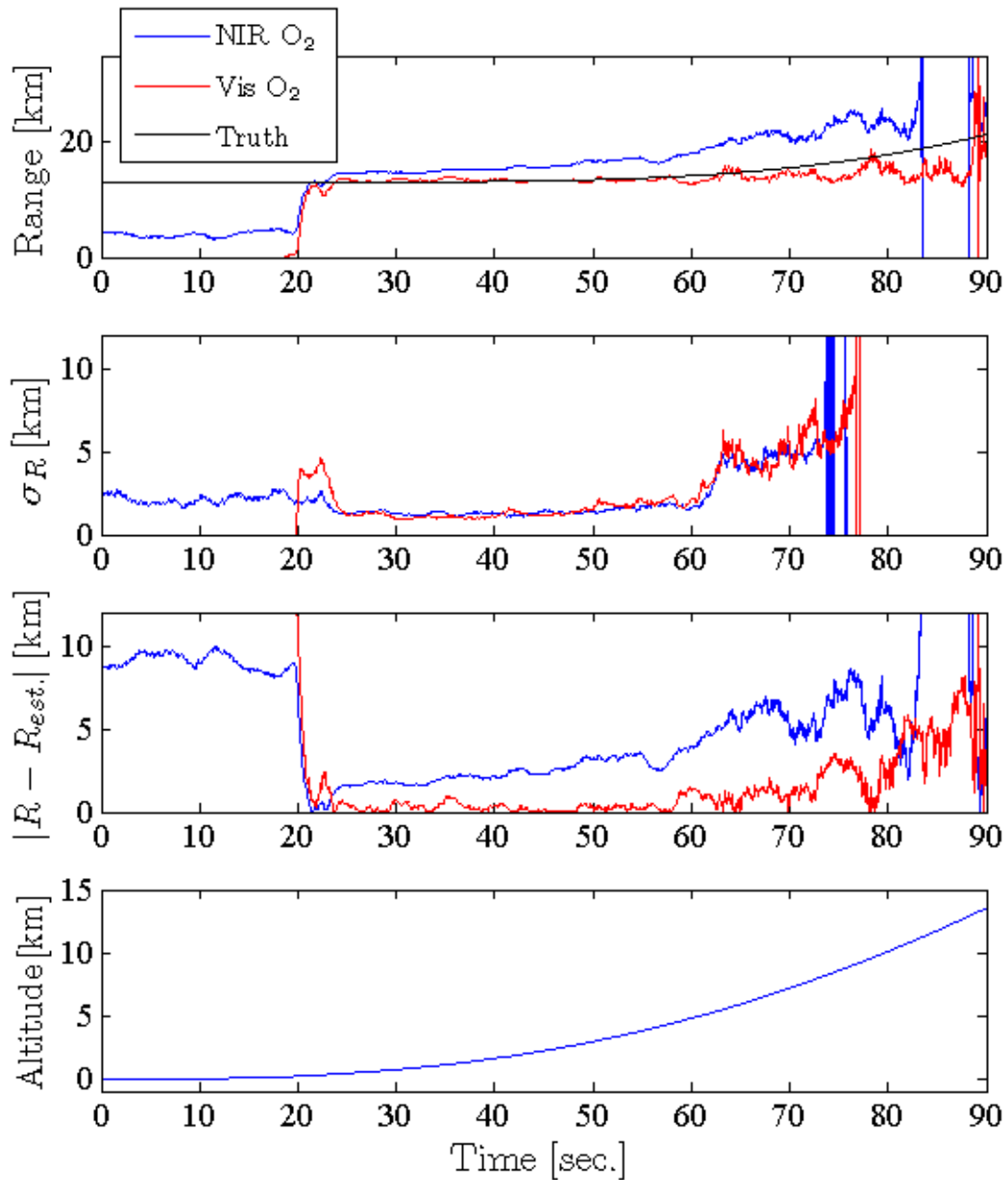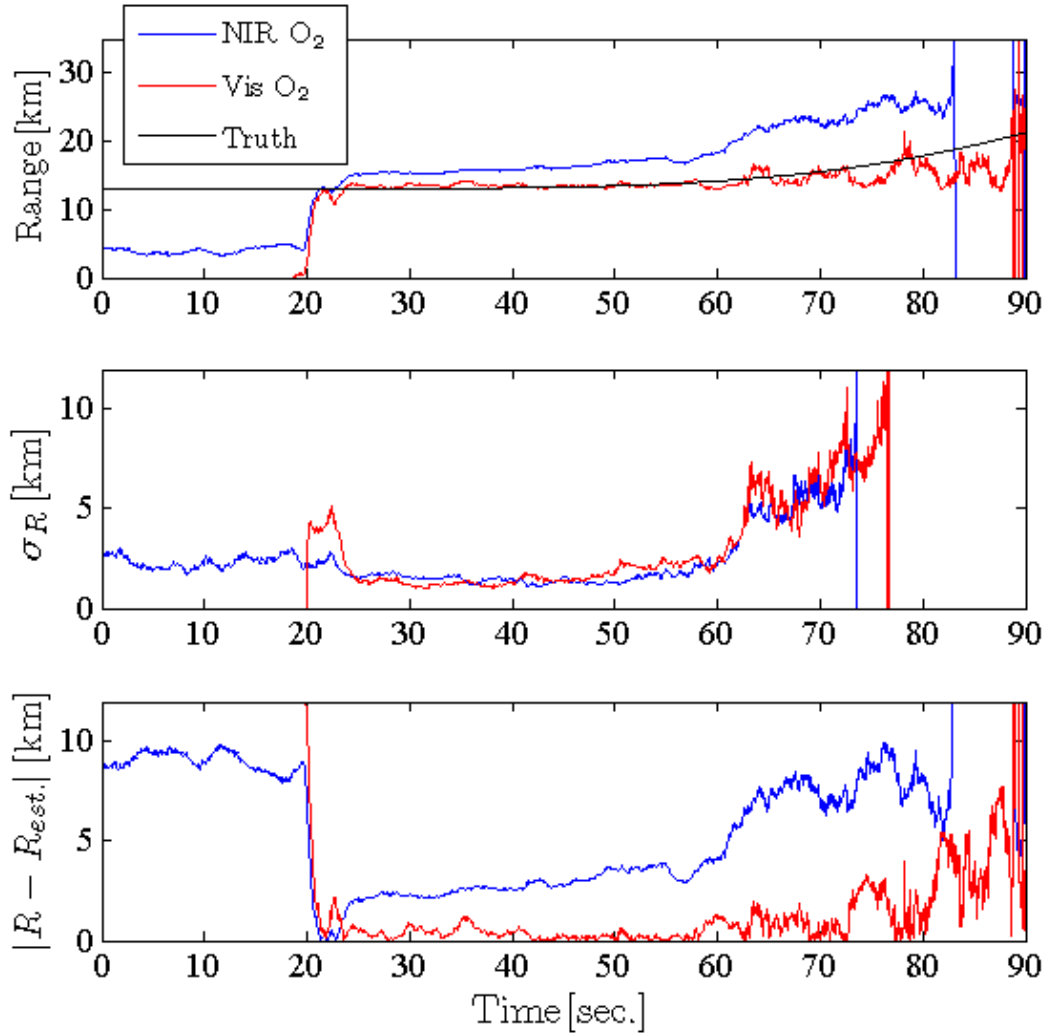
Figure 35. Top: Range estimates for each O_2 band of the Falcon 9 rocket during launch using a tropical atmospheric profile. The black line represents the true range between sensor and Falcon 9 after ignition. Middle: Uncertainties in range estimates for each O_2 band. The spurious lines after approx 70 seconds arise from interpolated $\bar{A}$ values outside of the given lookup table. Bottom: The absolute value of the difference between the true range and the estimated range, also referred to as the residual error. Note that these results look nearly identical to those produced in Figure 34.

model look nearly identical to those already shown in Figure 34. This result does not entirely rule out variations between referenced and actual O_2 concentration profiles as the cause of the NIR range bias. It may be possible that there was a significant concentration boundary layer at low altitudes over the tracking site that was not accounted for in either referenced atmospheric profiles. Furthermore, radiances reflected off the dense Florida vegetation and scattered into the observation path may be non-negligible in this application.

Finally, it was crucial to use the sensor zenith angles in the interpolation of range from the lookup tables shown Figures 12 and 13. This is because even though the Falcon 9 was getting further away from the MR-304, it was increasing with altitude (bottom of Figure 34), thus traveling through exponentially thinning atmosphere. The projected slope of $\bar{A}$, Figure 14, predicted a maximum of 90 seconds of viable range estimation, which is exactly the duration of good range estimates shown in Figure 34. Ultimately, the range estimation limiting factor was the rocket leaving the atmosphere.

4.2.2   Systematic Error: Analysis and Compensation.

Based on the results shown in Figures 34 and 35, it is apparent that there is a differential systematic error affecting the NIR O_2 band and not the Vis O_2 band. This systematic error manifests itself in a range bias for the NIR range estimates. The fact that one band produced a range estimate shifted with respect to the other is a puzzling result. Both frequency ranges in the separate oxygen bands were observing the same source, through the same atmospheric path, and with the same optical train. However, this bias result is clearly observed so there must be a root cause, either physical or analytical.

A numerical test to probe the sensitivity of the range estimation process to sys-

57
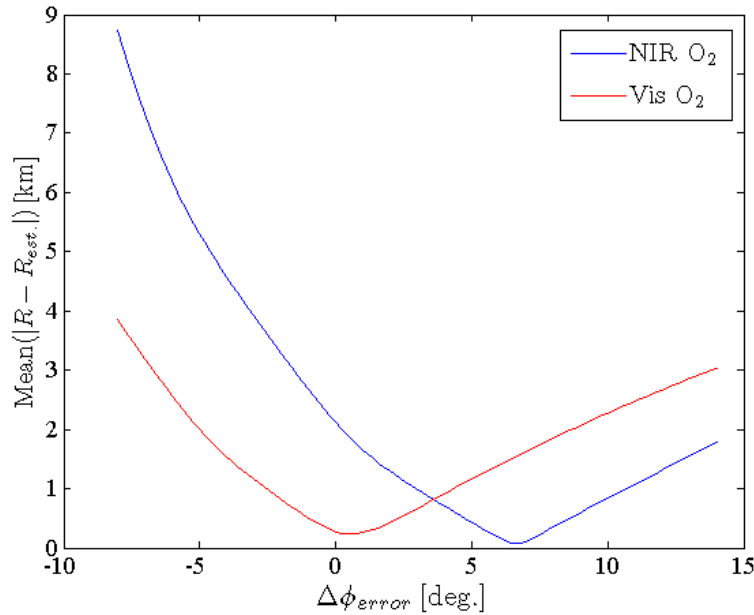
Figure 36. Plot of residual range error averaged over the first 30 seconds of Falcon 9 observation versus a systematically induced zenith angle offset. Note that the minimum residual range error occurs at $+0.4$ degrees for the Vis O_2 band, while the minimum residual occurs at $+6.4$ degrees for the NIR O_2 band. It is important to remember that these two oxygen bands were measured by the same instrument, the MR-304.

tematic errors was performed by inducing a zenith angle error of varying magnitude and sign. Figure 36 shows the magnitude of the residual range error averaged over the first 30 seconds of Falcon 9 acquisition versus an induced zenith angle offset. Surprisingly, the Vis O_2 band has minimum residual error at a zenith angle offset of $+0.4$ degrees, while the NIR O_2 band has a minimum at $+6.4$ degrees. Clearly the MR-304 could not be pointed incorrectly by two different angular amounts simultaneously. A zenith angle error in the instrumentation would show up either in both bands or not at all. Therefore, zenith angle error is not the root cause of the NIR bias, but is rather an alternative way to view the effects of this systematic error.

A zenith angle correction can be applied to the range estimates by taking the minimum residual error values in Figure 36 and simply shifting the measured zenith angles by $+6.4$ degrees for the NIR O_2 band and $+0.4$ degrees for the Vis O_2 band.

58
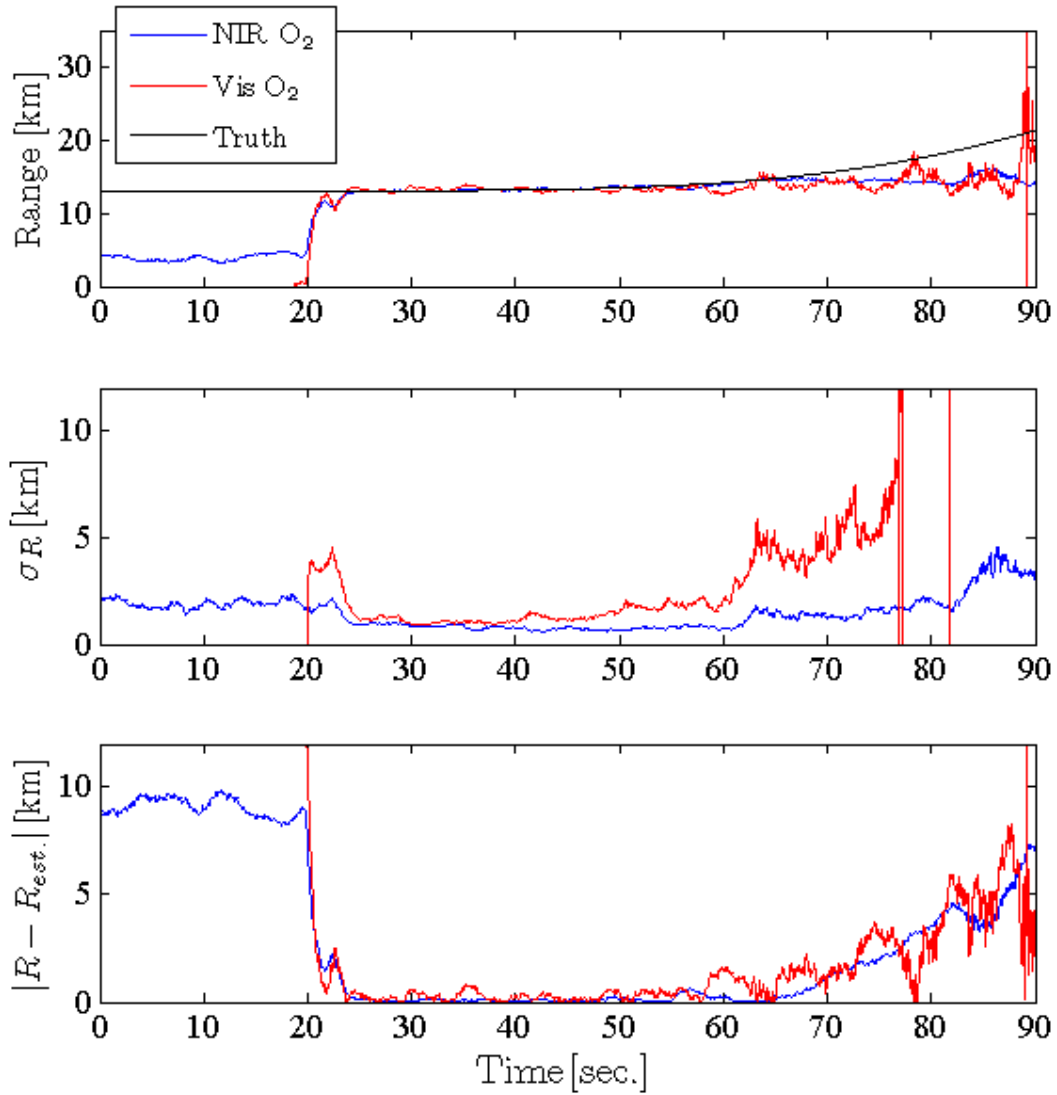
Figure 37. Top: Range estimates for each O_2 band of the Falcon 9 rocket during launch using a 1976 U.S. standard atmosphere and an applied zenith angle offset determined from Figure 36. The black line represents the true range between sensor and Falcon 9 after ignition. Middle: Uncertainties in range estimates for each O_2 band. Bottom: The absolute value of the difference between the true range and the estimated range, also referred to as the residual error. Note that the residual error for the NIR O_2 band dropped to approximately 1 % error by applying the zenith angle offset.

The corrected range estimates for the Falcon 9 test are shown in Figure 37. Notice that the NIR range bias has been completely removed with this method. Also, the range error dropped to approximately $3-4\%$ for the Vis O_2 band and $1-2\%$ for the NIR O_2 band. While the exact nature of this differential systematic error is unknown, it will certainly be the focus of future research in the field of MPR. None the less, these are amazingly accurate results and highlight the potential for real world applications of missile detection and defense.

4.2.3 Near-Real-Time Computation.

The computer time required to process the recorded interferograms was calculated the with the Matlab script given in Appendix C, using the 'tic toc' commands. It was assumed in the timing process that the required $\bar{A}$ lookup tables were preloaded into memory, the weather conditions during launch were already known, and that the interferograms and mount data for the entire launch were readily available for computation. A persistent effort was given towards optimizing the Matlab code presented in Appendix C.

For a 64-bit laptop running Matlab with 4 gigabytes of RAM and a duo-core 2 GHz processor, it was found that the process took 0.0660 seconds to calculate one range estimate from one interferogram. Figure 38 shows the breakdown of sub-processes and their computational time in seconds per frame. The section labeled "Interferograms" includes reading the recorded MR-304 data into Matlab and performing a one dimensional fast Fourier transform (FFT1d) to convert the interferogram to a spectrum. "Absorption" refers to the process of calculating $\bar{A}$ and $\sigma_{\bar{A}}$ for both bands from the given spectrum, Appendix A. The computation time required to interpolate range within the two dimensional lookup table, given $\bar{A}$ and ϕ, is labeled "Interpolation". Finally, "Mount Data" refers to the process of reading in the mount data and

60
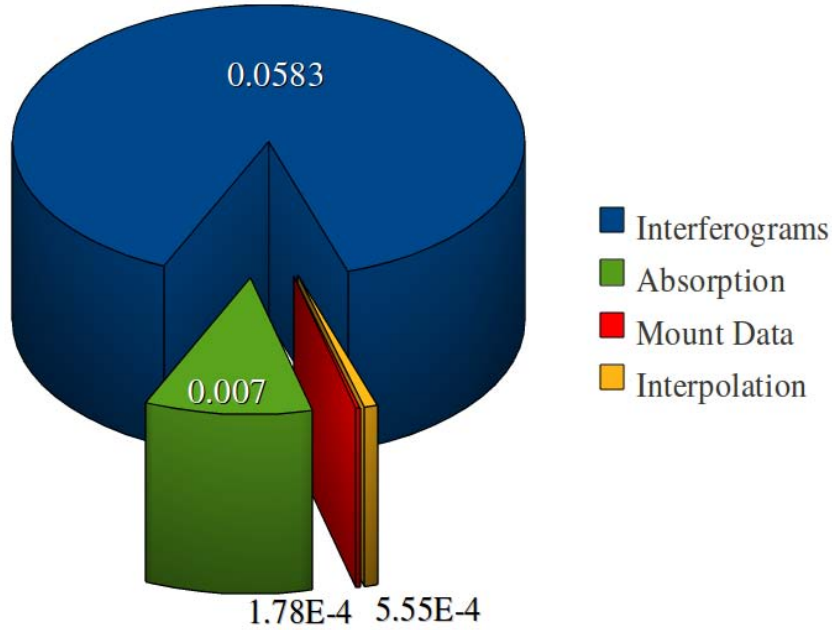
Figure 38. Breakdown of subprocess computational time per frame required to generate one range estimate from one measured interferogram. Numbers displayed in the pie chart have units of seconds per frame. Times were calculated by the algorithm in Appendix C.

matching the sampled mount time to the MR-304 time.

It is apparent that the majority of the processing time is spent generating spectra from the interferograms. This is a process unique to the interferometer design of the FTS. A prototype MPR system could avoid this expensive computation by incorporating a dispersive spectrometer design or, potentially, a sensor based upon band pass filters. Additionally, the total computation time per frame can be greatly reduced by exporting the Matlab processing code to a compilable language, such as FORTRAN or C++. There is also a likely gain by switching to a Unix based platform instead of running MPR code in a MS Windows based environment.

4.3 Summary

The presented results corroborated previous MPR research, [7]; for ranges less than one kilometer, the NIR O_2 band can be used to accurately estimate range with an error less than 3%. Within this range, it was also shown that the Vis O_2 band did not provide accurate range estimates, because of weaker absorption. The most accurate result for the Vis band had 15% error at $900\,\mathrm{m}$. These results were proven with the Smoky SAM test and the SRT.

The Falcon 9 rocket launch observation showed that the Vis O_2 band can provide accurate range estimates, given a long enough absorption path. The dynamic range from sensor to Falcon 9 was greater than $13\,\mathrm{km}$ throughout launch. For the first 30 seconds of observed flight, the Vis band yielded accurate range estimates with errors less than 8%. The NIR O_2 band, however, never had less than 20% error, possibly due to in-band saturation. After making corrections for a band specific zenith angle offset, range estimates had less than 4% error for the Vis band and less than 2% error for the NIR band. Degradation in range estimates 70 seconds into flight were primarily attributed to the Falcon 9 gaining altitude, resulting in a decrease of absorbing species along the observation path.

Finally, the computational time required to generate one estimate of range was reduced from 130 seconds to 0.066 seconds. This was accomplished by performing the intensive LBLRTM calculations prior to observation and storing the data in a two dimensional lookup table. The subprocesses in the range estimation were also timed during evaluation. It was found that the majority of the range processing time was spent reading the inteferograms and converting them to spectra via a FFT1d. Future designs of MPR systems could avoid this time sink by using a dispersive spectrometer or a band pass filter design.

V. Conclusion

This research focused on using spectra from emissive rocket plumes to estimate range from sensor to target. Band averaged absorption was calculated from the observed plume spectra and compared to modeled absorption from LBLRTM. Absorption within an atmospheric NIR oxygen band was targeted, because the NIR band is spectrally isolated from other absorbing species and it is weak enough not to saturate over short path lengths. For a full scale static rocket motor at 900 m and a small model SAM at 405 m, it was found that the NIR O_2 band accurately estimated range with an error less than 3 %. For a Falcon 9 rocket launch with an initial range of 13 km, the NIR O_2 band overestimated range with a bias of at least 2 km. Falcon 9 range estimates had an error greater than 20 % for the duration of the flight. Saturation within the NIR O_2 band may have contributed to the larger error at 13 km. Therefore, the NIR O_2 band provided accurate range estimates to within 3 % for ranges between 400 and 900 m, while ranges greater than 13 km were estimated with an error greater than 20 %.

A second oxygen band in the visible spectrum was also used to estimate range for comparison to the NIR O_2 band. The Vis O_2 band is weaker than the NIR O_2 band, so it will not saturate until much longer path lengths than the NIR band. For ranges less than 900 m, the Vis band produced much less accurate range estimates than the NIR band. The Vis O_2 band yielded estimates with a 77 % error at 405 m and a 15 % error at 900 m. The larger error is attributed to the weak absorption within the Vis band at these ranges. Alternatively, the Vis O_2 band was used to accurately estimate dynamic range to the Falcon 9 rocket; error was found to be less than 8 % for at least 30 seconds after launch. During this 30 second time period the Falcon 9 climbed from 200 meters to 4 kilometers in altitude with a range increase from 13.1 to 13.5 kilometers.

Upon analysis of the bias in the NIR O_2 range estimates for the Falcon 9 test, it was found that residual range error was minimized by applying a zenith angle offset of $+0.4$ degrees for the Vis O_2 band and $+6.4$ degrees for the NIR O_2 band. This method was found to completely remove the bias in the NIR band, while significantly increasing range accuracy to less than 4% error for the Vis O_2 band and less than 2% error for the NIR O_2 band. While the root cause of this systematic error is still to be determined with future research, these results highlight the potential accuracy of a MPR system for future applications of missile detection and defense.

It was also demonstrated that there is potential to extend the method of MPR using band averaged absorption for near-real-time range estimation. The dependency upon running radiative transfer models during range estimation was removed by running LBLRTM beforehand (without *a priori* knowledge of the target or trajectory) and pre-calculating a two dimensional absorption lookup table based on range and sensor zenith angle. By incorporating an $\bar{A}$ lookup table, the time to generate one range estimate from one observed interferogram was measured to be 0.0660 seconds. Finally, recommendations for further decreasing range estimation time were also discussed.

5.1 Future Recommendations

The Falcon 9 rocket observation was the first successful dynamic range application of band averaged absorption for MPR. Based on these results, additional tests at various initial ranges are recommended. The horizontal range at which the Vis O_2 band provides more accurate range estimates than the NIR O_2 band will be target dependent. This trade-off may occur somewhere in the range of $1-13$ km. Therefore, both NIR and Vis O_2 bands should be used in conjunction during passive ranging estimation with a weighting criteria that seamlessly shifts between the two bands

depending upon range.

This work could potentially extend to an aerial MPR platform, either in a plane or satellite based sensor design. An important consideration for long range applications is the benefit in observing along a slant angle, so that a thicker atmospheric path is sampled. For a proposed sensor geometry the slope of $\bar{A}$ versus range must be nonzero over the ranges of interest in order to achieve accurate estimates. The lookup table used in this research can be extended for aerial use by adding sensor altitude as a third dimension.

The Bomem MR-304 spectrometer was not the optimal sensor for this application. A FTS is without parallel when it comes to passive high spectral resolution sensing. However, the presented results were achieved with a spectral resolution of $4\,cm^{-1}$. It is possible a lower resolution may have achieved such results. Therefore, a dispersive spectrometer, designed for maximum efficiency at the oxygen absorption frequencies, would reduce sensor size and greatly speed up range estimation time. This is because there are no scanning optics in a dispersive spectrometer, and frequencies are directly mapped to pixel location (no Fourier transforms).

Finally, there is also potential to revise and modify the band pass filter system tested by Anderson, [1]. A MPR system based upon band pass filters has the benefit of compact design and is generally less expensive than a spectrometer. A filter based sensor also maintains the two dimensional spacial features of the scene without having to scan the sensor across the area of interest. In conclusion, a sensor designed specifically for the purpose of MPR may produce more accurate range estimates than the results presented in this thesis.

Appendix A. Function to Calculate $\bar{A}$

A Matlab function that calculates band averaged absorption $(\bar{A})$ for the NIR and Vis O$_2$ bands. This function requires an input spectrum and its corresponding wavenumber axis.

```
function [Abar1st,Abar2nd,Abar1hi,Abar1low,Abar2hi,Abar2low,SNRout1,SNRout2]
          = AbarFunct(f,Spect,sum_method)
% [Abar1st,Abar2nd,Abar1hi,Abar1low,Abar2hi,Abar2low,SNRout1,SNRout2]=
%    AbarFunct(f,Spect,sum_method)
% A function to calculate band averaged absorption of the NIR and Visible
% oxygen bands for use in passive ranging.
%
% AbarFunct.m:  Version 1.0      03Nov2010
%               Version 1.1      15Feb2011
%                                (updated to include Matlab uncertainties
%                                for polyfit command)
%               Version 1.2      28Feb2011
%                                (updated to include proper derivation of
%                                uncertainty)
%
% Inputs: f = frequency axis in [cm^-1] units
%         Spect = measured spectrum [arbitrary units]
%         sum_method --> flag specifying which summation method to use when
%                         calculating Abar.
%
% Outputs:  Abar1st = band averaged absorption (Abar) for NIR oxygen band
%           Abar2nd = Abar for visible oxygen band
%           Abar(1 or 2)(hi or low) = upper and lower bounds on Abar for
%             approximating 68% confidence interval
%           SNRout(1 or 2) = approx SNR from out-of-band data

if nargin<3, sum_method=1; end
if isempty(sum_method)==1, sum_method=1; end
if sum_method~=2, sum_method=1; end
%display(['sum_method = ',num2str(sum_method)]);

%% First O2 band (NIR)
freq_bounds=[12785,12843,13200,13360]; % Define out-of-band regions
i_bnds=zeros(1:4);
for j=1:4;
    err=abs(f-freq_bounds(j));
    i_bnds(j)=find(err==min(err),1,'first');
```

66

```
end

Spect=Spect(:);
% clip out an array of only the out-of-band Transmission data
ii=[i_bnds(1):i_bnds(2),i_bnds(3):i_bnds(4)];
Spectout=Spect(ii,:);
fout=f(ii);  fout=fout(:);

% locate the desired in-band regions
freq_bounds_in=[13122,13200];
i_bnds_in=zeros(1:2);
for j=1:2;
    err_in=abs(f-freq_bounds_in(j));
    i_bnds_in(j)=find(err_in==min(err_in),1,'first');
end
% Now clip the in-band part to use in finding band avg
fin=f(i_bnds_in(1):i_bnds_in(2));
Spectin=Spect(i_bnds_in(1):i_bnds_in(2),:);


% find baseline by fitting to out of band data
[basefit,S,mu]=polyfit(fout,Spectout(:),2);
[baseline,delta]=polyval(basefit,fin,S,mu);

if sum_method==1,
    A=1 - Spectin(:)./baseline(:);
    Abar=trapz(A);
    Abar1st=Abar/(length(fin));
elseif sum_method==2,
    auc = sum(baseline);
    abc = sum(baseline-Spectin(:)');
    Abar1st = abc/auc;
else display('There is an error in the summation process....');
end

baseout=polyval(basefit,fout,[],mu);% a baseline through out of band data
zeromeanout=Spectout-baseout;        % get rid of the curve (zero mean)
std_dev_sig=std(zeromeanout);        % std-deviation of out-of-band data

SNRout1=mean(Spectout)/std_dev_sig;   % approx SNR from out-of-band data

% calculation of uncertainty (see thesis for discussion)
Abar_uncert=sqrt(std_dev_sig.^2+(1-Abar1st).^2.*mean(delta).^2)./...
    mean(baseline);
Abar1hi=Abar1st+Abar_uncert;
Abar1low=Abar1st-Abar_uncert;
```

67

```matlab
%% Second O2 band (Visible)
% One sided out-of-band baseline, due to water band overlap with P-branch

% locate the desired out-of-band region
freq_bounds2=[14590,14900];
for j=1:2;
    err=abs(f-freq_bounds2(j));
    i_bnds(j)=find(err==min(err),1,'first');
end

% clip out an array of only the out-of-band Transmission data
ii=[i_bnds(1):i_bnds(2)];
Spect2out=Spect(ii,:);
f2out=f(ii);   f2out=f2out(:);

% locate the desired in-band regions
freq_bounds_in2=[14527,14566];
for j=1:2;
    err_in=abs(f-freq_bounds_in2(j));
    i_bnds_in(j)=find(err_in==min(err_in),1,'first');
end
% Now clip the in-band part to use in finding band avg
f2in=f(i_bnds_in(1):i_bnds_in(2));
Spect2in=Spect(i_bnds_in(1):i_bnds_in(2),:);



% find baseline by fitting to out of band data
[basefit2,S,mu]=polyfit(f2out,Spect2out(:),1);
[baseline2,delta]=polyval(basefit2,f2in,S,mu);

if sum_method==1,
    A=1 - Spect2in(:)./baseline2(:);
    Abar2nd=trapz(A);
    Abar2nd=Abar2nd/(length(f2in));
elseif sum_method==2,
    auc = sum(baseline2);
    abc = sum(baseline2-Spect2in(:)');
    Abar2nd = abc/auc;
else display('There is an error in the summation process....');
end

baseout=polyval(basefit2,f2out,[],mu);% a baseline through out of band data
zeromeanout=Spect2out-baseout;         % get rid of the curve (zero mean)
std_dev_sig=std(zeromeanout);          % std-deviation of out-of-band data
```

```
SNRout2=mean(Spect2out)/std_dev_sig;    % approx SNR from out-of-band data

% calculation of uncertainty (see thesis for details)
Abar_uncert=sqrt(std_dev_sig^2+(1-Abar2nd).^2.*mean(delta).^2)./...
    mean(baseline2);
Abar2hi=Abar2nd+Abar_uncert;
Abar2low=Abar2nd-Abar_uncert;
```

Appendix B. Script to Create a Lookup Table for $\bar{A}$

This is the Matlab script used to generate a lookup table for $\bar{A}$. This script loops through given values of range and zenith angle, and uses LBLRTM to generate transmission curves for each run. Allow for several hours of computation time on a standard 2 GHz dual-core laptop or desktop computer.

```
%% angle_range_O2.m
%  An m-script designed to create a 3-d lookup table for both oxygen bands
%  with dimensions of (Range,Zenith Angle,Abar). Sensor altitude above
%  sea level is an important parameter in building an accurate table.
%  Current settings are optimized for Cape Canaveral altitude conditions
%  (1 meter above sea level).

% Set up path
path(pwd,path);
if ~exist('LBLRTM_DIR','var'); [LBLRTM_DIR,LBLCODE,OUT_DIR]=setglobals; end

warning off MATLAB:polyfit:RepeatedPointsOrRescale;

%Test site parameters (some parameters may not be used in this script)
inp.alt=0.001;                     %km
inp.temp.a=25.7;                   %Celsius
inp.temp.b=inp.temp.a+273.15;      %Kelvin
inp.press.a=992.5;                 %hecto Pascals
inp.press.b=inp.press.a*0.02953;   %inches of mercury
inp.press.c=inp.press.a*0.000986923;  %atmopheres
inp.dewpoint=17.38;                %celsius
inp.zenithang=89;                  %viewing angle, degrees from zenith

%% 1st O2 band
nu_min=12600;   nu_max=14000;
N = 65536/2 / 2 + 1; %Divide by 2 for oversampling, then divide by 2 for MOPD
MOPD = 632.816e-7 * N;
% f = nu_min:0.1:nu_max;
%% 2nd O2 band

nu_min2=13600;   nu_max2=15000;

%% Calculate for various angles

angle=[0.1,5,10,15,20,25,30,35,40,45,50,55,60,65,70,75,80,85,89];
%angle=[10];
                                   % angle values to iterate through
```

70

```matlab
%% 1A) Compute LBLRTM transmission for several different ranges
R = [.25,.5,.75,1,2,3,5,7,10,15,20,30,40,50,60,70,80,90,100,110,120,130,...
    140,150,160,180,200,220,260,300];
                                        % Range values to iterate through

Abar=zeros(length(angle),length(R));
Abar2=Abar;
for kk=1:length(angle);
  for j=1:length(R);
    disp(' ');
    disp([' --- For R=',num2str(R(j)),' km ---']);
    lblrtm = gen_TP5_struct('pathlength',R(j),'Altitude',inp.alt,...
        'temperature',inp.temp.b,'pressure',inp.press.c,'ZenithAngle',...
        angle(kk),'nu_max',nu_max,'nu_min',nu_min,'MOPD',MOPD,...
        'apodizer','tri');
    [f,trans] = compute_transmittance(lblrtm);
    T(:,j)=trans(:);
  end
end


%% 1B) Compute LBLRTM band average absorption for each range

% locate the desired out-of-band regions
freq_bounds=[12785,12843,13200,13360];
for j=1:4;
    err=abs(f-freq_bounds(j));
    i_bnds(j)=find(err==min(err),1,'first');
end

% clip out an array of only the out-of-band Transmission data
ii=[i_bnds(1):i_bnds(2),i_bnds(3):i_bnds(4)];
Tout=T(ii,:);
fout=f(ii);  fout=fout(:);

% locate the desired in-band regions
freq_bounds_in=[13122,13200];
for j=1:2;
    err_in=abs(f-freq_bounds_in(j));
    i_bnds_in(j)=find(err_in==min(err_in),1,'first');
end
% Now clip the in-band part to use in finding band avg
fin=f(i_bnds_in(1):i_bnds_in(2));
Tin=T(i_bnds_in(1):i_bnds_in(2),:);

for j=1:length(R);
```

71

```matlab
    % find baseline by fitting to out of band data
    basefit=polyfit(fout,Tout(:,j),1);
    baseline=polyval(basefit,fin);
%       auc = sum(baseline);
%       abc = sum(baseline-Tin(:,j)');
%       Abar(j) = abc/auc;
      % Alternative way to calculate Abar (nearly identical to uncommented
      % Abar method).
    A=1 - Tin(:,j)./baseline(:);
    Abar(kk,j)=trapz(A)/length(fin);
end

%% 2A) Compute LBLRTM transmission for several different ranges
for j=1:length(R);
    disp(' ');
    disp([' --- For R=',num2str(R(j)),' km ---']);
    lblrtm = gen_TP5_struct('pathlength',R(j),'Altitude',inp.alt,...
        'temperature',inp.temp.b,'pressure',inp.press.c,'ZenithAngle',...
        angle(kk),'nu_max',nu_max2,'nu_min',nu_min2,'MOPD',MOPD,...
        'apodizer','tri');
    [f2,trans] = compute_transmittance(lblrtm);
    T2(:,j)=trans(:);
end

%plot(f2,T2(:,30));

%% 2B) Compute LBLRTM band average absorption for each range

% locate the desired out-of-band regions
freq_bounds2=[14590,14900];
for j=1:2;
    err=abs(f2-freq_bounds2(j));
    i_bnds(j)=find(err==min(err),1,'first');
end

% clip out an array of only the out-of-band Transmission data
ii=[i_bnds(1):i_bnds(2)];
T2out=T2(ii,:);
f2out=f2(ii);   f2out=f2out(:);

% locate the desired in-band regions
freq_bounds_in2=[14527,14566];
for j=1:2;
    err_in=abs(f2-freq_bounds_in2(j));
    i_bnds_in(j)=find(err_in==min(err_in),1,'first');
end
```

72

```matlab
% Now clip the in-band part to use in finding band avg
f2in=f2(i_bnds_in(1):i_bnds_in(2));
T2in=T2(i_bnds_in(1):i_bnds_in(2),:);

for j=1:length(R);
    % find baseline by fitting to out of band data
    basefit2=polyfit(f2out,T2out(:,j),2);
    baseline2=polyval(basefit2,f2in);
%     auc = sum(baseline);
%     abc = sum(baseline-Tin(:,j)');
%     Abar(j) = abc/auc;
    A=1 - T2in(:,j)./baseline2(:);
    Abar2(kk,j)=trapz(A)/length(f2in);
end

figure(1);
plot(R,Abar(kk,:),R,Abar2(kk,:),'--');
title(num2str(kk));
end
% Now you can save the lookup table by hand or insert a command here to
% auto-save to a specified directory.
```

Appendix C. Script to Calculate Range from Sensor to Rocket

```
%% RapidRangeEst.m
%   This script is designed to simulate a near real time rocket range
% estimation system. Once the interferograms become available, this script
% makes use of a saved 3-d lookup table of dimensions (range,zenith angle,
% band averaged absorption) for both NIR and visible oxygen absorption bands.

% RapidRangeEst.m:  Version 1.0      03Nov2010

% Needs Inputs:
%   -    Bomem interferograms
%   -    Metrology data, specifically; Temp(c), Pressure(hPa), Humidity(%)
%   -    Saved 3-d lookup table generated by LBLRTM or FASCODE for both
%        Oxygen bands centered at 762nm and 690nm
%   -    Truth value of range for comparison (if available)
%   -    Oxygen column density from the Tape 6 file generated by LBLRTM
%        and used for atmospheric corrections

% Needs functions:
%   -    importBomem.m (with entire supporting Bomem Matlab library)
%        [reads in Bomem interferograms and calculates observed spectra]
%   -    metars.m [computes oxygen density at sensor]
%   -    AbarFunct.m

%clear all;
%clc;
clear Abar1st Abar2nd Abar1low Abar1hi Abar2low Abar2hi range1stO2 range2ndO2;
close all;
warning off MATLAB:polyfit:RepeatedPointsOrRescale;

%% Load lookup table

if ~exist('tablename','var');
[tablename,tablepthname]=uigetfile('*.mat','select lookup table');
                                % angle_range_O2_sealevel.mat
load([tablepthname,tablename]);
end

%% Input truth range and atmospheric parameters

%Test site parameters              (Falcon9, Kennedy SC atmosphere data)
inp.truthrange=13.0;                %km
```

```matlab
inp.alt=.002;                              %km
inp.temp.a=12.5;                           %Celsius
inp.temp.b=inp.temp.a+273.15;              %Kelvin
%inp.press.a=844.9;                         %hecto Pascals
%inp.press.b=inp.press.a*0.02953;           %inches of mercury
inp.press.b=30.14;                         %inches of mercury
%inp.press.c=inp.press.a*0.000986923; %atmopheres
inp.dewpoint=2.44;                         %celsius
inp.zenithang=89;                          %viewing angle, degrees from zenith


%NoxLBL=(1.1244604E+23)*100^2/250;  %1/m^3  (Utah, what LBLRTM used for ref.)
% #density of Oxygen from LBLRTM (1/m^3)=(column density from Tape 6 file
% in 1/cm^2)*convert to 1/m^2 / 250 meter slant path
%             [Look up from Tape 6 file]
NoxLBL=(1.2961360E+23)*100^2/245.357;  %(Cape Canaveral/Kennedy Space Center)


Nox=metars(inp.press.b,inp.temp.a,inp.dewpoint,inp.alt,inp.alt);
                          %1/m^3 (data from test site)


% This ratio will be multiplied to the range estimate for a more accurate
% result -->
atmoscrt=Nox/NoxLBL;


%% Load the Bomem data and choose parameters

% Read in 1 data frame from the Bomem data FYI.
if ~exist('Bmfname','var');
[Bmfname,Bmpthname]=uigetfile('*.Igm','select Bomem interferegram data');
end
[XA,YA,XB,YB,IA,IB,t,Hdr,Dr] = importBomem([Bmpthname,Bmfname],0);
display(['Description of data -->  ', Hdr.DataFileDescription]);
display(['Number of measurements -->  ', num2str(Hdr.NbMeasurements)]);
display(['Number of Coadds -->  ', num2str(Hdr.NbCoadds)]);

% enter the number of frames desired for a running average
NumRunAve = input('How many frames do you want for a running average?'...
                ' (0 - 300 or so) ');
if isempty(NumRunAve)
    NumRunAve = 0;
end

% which summation method do you want to use
sumflag = input('Which summation method do you want to use? (1 or 2) ');

% use even sized bucket to avoid timing problems
if NumRunAve<0, NumRunAve=0; display(['Can not take a running average',...
```

75

```matlab
        ' with a negative frame number. NumRunAve = 0']);
end
if NumRunAve/2-round(NumRunAve/2) ~= 0;
    NumRunAve = NumRunAve+1;
end


% Load in all the Bomem spectral data. Skip this step if already loaded.
if exist('Spec','var')~=1,
    tic;
    Spec=zeros(Hdr.NbMeasurements,size(YA,2));
    timestamp=zeros(1,Hdr.NbMeasurements);
    h = waitbar(0,'Loading and transforming Bomem data...');
    for jd=1:Hdr.NbMeasurements;
        [XA,Spec(jd,:),XB,YB,IA,IB,timestamp(1,jd),Hdr,Dr] =importBomem(...
            [Bmpthname,Bmfname],jd-1);
        waitbar(jd/Hdr.NbMeasurements);
    end
    timestamp=timestamp-1291766400; %subtract Unix Time for 8Dec2010 12:00am
    timer.bomem=toc/Hdr.NbMeasurements;
    close(h);
end


% Only pass the frequencies that are of interest to save computer time
WNindexlo = find(abs(12000-XA)==min(abs(12000-XA)),1,'first');
WNindexhi = find(abs(15000-XA)==min(abs(15000-XA)),1,'first');

%% Section for no running average
if NumRunAve==0,
    tic; % start Abar timer
    % initialize variables for faster loop
    Abar1st=zeros(size(timestamp)); Abar2nd=zeros(size(timestamp));
    Abar1hi=zeros(size(timestamp)); Abar1low=zeros(size(timestamp));
    Abar2hi=zeros(size(timestamp)); Abar2low=zeros(size(timestamp));

    % Calculate Abar with errorbars for both oxygen bands
    for id=1:Hdr.NbMeasurements;
        [Abar1st(id),Abar2nd(id),Abar1hi(id),Abar1low(id),Abar2hi(id),...
            Abar2low(id),SNRout1(id),SNRout2(id)]=AbarFunct(XA(1,...
            WNindexlo:WNindexhi),abs(real(Spec(id,WNindexlo:WNindexhi)...
            )),sumflag);
    end

    timer.abar=toc/Hdr.NbMeasurements; % end Abar timer

    % Calculate range estimate using lookup table with interpolating
```

76

```
% functions
tic; % start interpolation timer
range1stO2=zeros(size(Abar1st)); range2ndO2=range1stO2;
range1stO2=interp1(interp2(angle,R,Abar',inp.zenithang,R,'spline'),...
    R,Abar1st,'spline');
range2ndO2=interp1(interp2(angle,R,Abar2',inp.zenithang,R,'spline')...
    ,R,Abar2nd,'spline');
timer.interp=toc; % end timer

% Calculate the standard deviation in Abar (68% confidence interval)
Abar1stsigma=zeros(size(Abar1st)); Abar2ndsigma=Abar1stsigma;
Abar1stsigma=Abar1hi-Abar1low;
Abar2ndsigma=Abar2hi-Abar2low;

% Now calculate the standard deviation in the range estimates (68%
% confidence interval)
range1stsigma=zeros(size(Abar1st)); range2ndsigma=range1stsigma;
range1stsigma=interp1(interp2(angle,R,Abar',inp.zenithang,R,'spline')...
    ,R,Abar1hi,'spline')-interp1(interp2(angle,R,Abar',inp.zenithang...
    ,R,'spline'),R,Abar1low,'spline');
range2ndsigma=interp1(interp2(angle,R,Abar',inp.zenithang,R,'spline')...
    ,R,Abar2hi,'spline')-interp1(interp2(angle,R,Abar',inp.zenithang,...
    R,'spline'),R,Abar2low,'spline');

figure(1);
subplot(3,1,1);
plot(timestamp-timestamp(1,1),Abar1st,'b',timestamp-timestamp(1,1),...
    Abar2nd,'r');
ylabel('$\bar{A}$','interpreter','latex','fontsize',20);

subplot(3,1,2);
plot(timestamp-timestamp(1,1),Abar1stsigma,'b',timestamp-...
    timestamp(1,1),Abar2ndsigma,'r');
ylabel('$\sigma_{\bar{A}}$','interpreter','latex','fontsize',14);
legend('NIR','VIS','Location','Best');

subplot(3,1,3);
plot(timestamp-timestamp(1,1),SNRout1,'b',timestamp-timestamp(1,1),...
    SNRout2,'r');
ylabel('SNR','fontsize',14);
xlabel('time [sec]','fontsize',14);

%    figure(2);
%    subplot(2,1,1);
%    plot(timestamp-timestamp(1,1),range1stO2,'b',timestamp-...
%        timestamp(1,1),range2ndO2,'r');
```

```matlab
%       ylabel('Range [km]','fontsize',14);
%       legend('NIR','VIS','Location','Best');
%
%       subplot(2,1,2);
%       plot(timestamp-timestamp(1,1),range1stsigma,'b',timestamp-...
%           timestamp(1,1),range2ndsigma,'r');
%       ylabel('$\sigma_R\,[\mathrm{km}]$','fontsize',14,...
%           'interpreter','latex');
%       xlabel('time [sec]','fontsize',14);

else
%% Section for a specified running average

    tic; % start Abar timer
    % initialize variables for faster loop
    timestampRunAve=zeros(1,size(timestamp,2)-NumRunAve);
    Abar1st=zeros(size(timestampRunAve)); Abar2nd=zeros(size(...
        timestampRunAve));
    Abar1hi=zeros(size(timestampRunAve)); Abar1low=zeros(size(...
        timestampRunAve));
    Abar2hi=zeros(size(timestampRunAve)); Abar2low=zeros(size(...
        timestampRunAve));
    SNRout1=zeros(size(timestampRunAve)); SNRout2=zeros(size(...
        timestampRunAve));

    % Calculate Abar with errorbars for both oxygen bands
    for id=1:Hdr.NbMeasurements-NumRunAve;
        [Abar1st(id),Abar2nd(id),Abar1hi(id),Abar1low(id),Abar2hi(id),...
            Abar2low(id),SNRout1(id),SNRout2(id)]=AbarFunct(XA(1,...
            WNindexlo:WNindexhi),mean(abs(real(Spec(id:id+NumRunAve...
            ,WNindexlo:WNindexhi))),1),sumflag);
        timestampRunAve(id)=timestamp(1,id+NumRunAve/2);
    end
    timer.abar=toc/(Hdr.NbMeasurements-NumRunAve); % end Abar timer

    % Load mount data from Black Mace and match timescales to Bomems
    if exist('mnt','var')~=1,
        [Mntname,Mntpthname]=uigetfile('*.txt','select mount data');
    end
    tic;
    mnt=importdata([Mntpthname,Mntname]);
    % Convert mount GPS time into seconds of the day
    mnt.time=mnt.data(:,4)*3600+mnt.data(:,5)*60+mnt.data(:,6)+...
        mnt.data(:,7)/1000;
    % Match measured zenith angle to Bomem GPS time scale
    mnt.zenithang=90-interp1(mnt.time,mnt.data(:,9),timestampRunAve...
```

78

```matlab
                ,'spline');
% Predicted range from mount data
inp.range=interp1(mnt.time,mnt.data(:,21),timestampRunAve,'spline');
timer.mount=toc/size(mnt.data,1); %How long it took per data line
                                % to compute


tic; % start interpolation timer
% Calculate range estimate using lookup table with interpolating
% functions
range1stO2=zeros(size(Abar1st)); range2ndO2=range1stO2;
timecurves1=interp2(angle,R,Abar',mnt.zenithang',R,'spline');
timecurves2=interp2(angle,R,Abar2',mnt.zenithang',R,'spline');
for id=1:size(Abar1st,2);
range1stO2(id)=interp1(timecurves1(:,id),R,Abar1st(1,id))./atmoscrt;
range2ndO2(id)=interp1(timecurves2(:,id),R,Abar2nd(1,id))./atmoscrt;
if isnan(range1stO2(id))==1, range1stO2(id)=0; end
if isnan(range2ndO2(id))==1, range2ndO2(id)=0; end
end
timer.interp=toc/id; % end interpolation timer

% Calculate the standard deviation in Abar (68% confidence interval)
Abar1stsigma=zeros(size(Abar1st)); Abar2ndsigma=Abar1stsigma;
Abar1stsigma=Abar1hi-Abar1low;
Abar2ndsigma=Abar2hi-Abar2low;

% Now calculate the standard deviation in the range estimates (68%
% confidence interval)
range1stsigma=zeros(size(Abar1st)); range2ndsigma=range1stsigma;
for id=1:size(Abar1st,2);
range1stsigma(id)=interp1(timecurves1(:,id),R,Abar1hi(1,id))-...
    interp1(timecurves1(:,id),R,Abar1low(1,id));
range2ndsigma(id)=interp1(timecurves2(:,id),R,Abar2hi(1,id))-...
    interp1(timecurves2(:,id),R,Abar2low(1,id));
if isnan(range1stsigma(id))==1, range1stsigma(id)=0; end
if isnan(range2ndsigma(id))==1, range2ndsigma(id)=0; end

end


figure(1);
subplot(3,1,1);
plot(timestampRunAve-timestampRunAve(1,1),Abar1st,'b',timestampRunAve...
    -timestampRunAve(1,1),Abar2nd,'r');
ylabel('$\bar{A}$','interpreter','latex','fontsize',20);
```

79

```matlab
    subplot(3,1,2);
    plot(timestampRunAve-timestampRunAve(1,1),Abar1stsigma,'b',...
        timestampRunAve-timestampRunAve(1,1),Abar2ndsigma,'r');
    ylabel('$\sigma_{\bar{A}}$','interpreter','latex','fontsize',14);
    legend('NIR','VIS','Location','Best');

    subplot(3,1,3);
    plot(timestampRunAve-timestampRunAve(1,1),SNRout1,'b',timestampRunAve...
        -timestampRunAve(1,1),SNRout2,'r');
    ylabel('SNR','fontsize',14);
    xlabel('time [sec]','fontsize',14);

    figure(2);
    subplot(3,1,1);
    plot(timestampRunAve-timestampRunAve(1,1),range1stO2,'b',...
        timestampRunAve-timestampRunAve(1,1),range2ndO2,'r',...
        timestampRunAve-timestampRunAve(1,1),inp.range/1000,'k');
    ylim([0 40]);
    xlim([0 150]);
    ylabel('Range [km]','fontsize',14);
    legend('NIR','VIS','Truth Range','Location','Best');

    subplot(3,1,2);
    plot(timestampRunAve-timestampRunAve(1,1),range1stsigma,'b',...
        timestampRunAve-timestampRunAve(1,1),range2ndsigma,'r');
    ylabel('$\sigma_R\,[\mathrm{km}]$','fontsize',14,'interpreter','latex');
    ylim([0 40]);
    xlim([0 150]);

    subplot(3,1,3);
    plot(timestampRunAve-timestampRunAve(1,1),mnt.zenithang);
    xlim([0 150]);
    xlabel('time [sec]','fontsize',14);

end

timer.all=[timer.bomem timer.abar timer.interp timer.mount];
timer.sum=sum(timer.all);
display('Computation time, in seconds, for one frame is:' ); timer
```

Appendix D. Example of a Tape 5 Input File used in LBLRTM

This is an example of a Tape 5 input file used for LBLRTM to generate transmission plots of a specified frequency range. The below example is for observation along a 65 degree zenith slant angle through a $5\,\mathrm{km}$ atmospheric path length. Sensor altitude is $1\,\mathrm{m}$ above sea level. The specified frequency range is $13,400 - 15,200\,\mathrm{cm^{-1}}$.

```
$ WRITE_TP5 autofile-20101012-172738
 HI=1 F4=1 CN=1 AE=1 EM=0 SC=0 FI=0 PL=0 TS=0 AM=1 MG=0 LA=0 OD=0 XS=0    0    0
 13400.000 15200.000
     6    2    0    1    0    8
      0.001              65.000      5.000
      1.250
     1    0    0   10    0    0
%
```

Bibliography

[1] Anderson, Joel R. *Monocular Passive Ranging by an Optical System with Band Pass Filtering*. Master's thesis, Air Force Institute of Technology, 2010.

[2] Bransden, B. H. and C. J. Joachain. *Physics of Atoms and Molecules*. Pearson Education Limited, Essex, England, 2nd edition, 2003.

[3] Clough, S. A., M. W. Shephard, P. D. Brown, S. Boukabara, K. Cady-Pereira, M. J. Iacono, J. S. Delamere, and E. J. Mlawer. "Atmospheric radiative transfer modeling: a summary of the AER codes". *Journal of Quantitative Spectroscopy and Radiative Transfer*, 91:233–244, 2005.

[4] Draper, J. S., S. Perlman, C. K. Chuang, M. Hanson, L. Lillard, B. Hibbeln, and D. Sene. "Tracking and Identification of Distant Missiles by Remote Sensing". *IEEE Aerospace Applications Conference; Proceedings of*, volume 4, 333–341. Mar 1999.

[5] Elsasser, Walter M. "Mean Absorption and Equivalent Absorption Coefficient of a Band Spectrum". *Physical Review*, 54:126–129, 1938.

[6] Goody, R. M. and Y. L. Yung. *Atmospheric Radiation: Theoretical Basis*. Oxford University Press, New York, 2nd edition, 1989.

[7] Hawks, Michael R. *Passive Ranging Using Atmospheric Oxygen Absorption Spectra*. Ph.D. thesis, Air Force Institute of Technology, 2005.

[8] Jursa, Adolph S. (editor). *Handbook of Geophysics and the Space Environment*. Air Force Geophysics Laboratory, 4th edition, 1985.

[9] Macdonald, Douglas J. *Passive Ranging Using Infra-Red Atmospheric Attenuation*. Master's thesis, Air Force Institute of Technology, 2010.

[10] Petty, Grant W. *A First Course in Atmospheric Radiation*. Sundog Publishing, Madison, Wisconsin, 2004.

[11] Rothman, L. S. and *et al.* "The *HITRAN* 2004 molecular spectroscopic database". *Journal of Quantitative Spectroscopy & Radiative Transfer*, 96:139–204, 2005.

[12] Scriven, G. and N. Gat. *Advanced Monocular Passive Ranging (AMPR) for HALO II*. SBIR Phase II Final Report AFRL-PR-ED-TR-2008-0018, Opto-Knowledge Systems Inc., Torrance, Ca, 2008.

[13] Taylor, J. R. *An Introduction to Error Analysis*. University Science Books, Sausalito, California, 2nd edition, 1997.

[14] Wiscombe, W. J. and J. W. Evans. "Exponential-Sum Fitting of Radiative Transmission Functions". *Journal of Computational Physics*, 24:416–444, 1977.

REPORT DOCUMENTATION PAGE

Form Approved
OMB No. 0704–0188

1. REPORT DATE *(DD–MM–YYYY)*	2. REPORT TYPE	3. DATES COVERED *(From — To)*
24–03–2011	Master's Thesis	Aug 2009 — Mar 2011

4. TITLE AND SUBTITLE

Passive Ranging of Dynamic Rocket Plumes using Infrared and Visible Oxygen Attenuation

5a. CONTRACT NUMBER

5b. GRANT NUMBER

5c. PROGRAM ELEMENT NUMBER

6. AUTHOR(S)

Vincent, Robert A., Capt, USAF

5d. PROJECT NUMBER

10ENP956

5e. TASK NUMBER

5f. WORK UNIT NUMBER

7. PERFORMING ORGANIZATION NAME(S) AND ADDRESS(ES)

Air Force Institute of Technology
Graduate School of Engineering and Management (AFIT/EN)
2950 Hobson Way
WPAFB OH 45433-7765

8. PERFORMING ORGANIZATION REPORT NUMBER

AFIT/GAP/ENP/11-M11

9. SPONSORING / MONITORING AGENCY NAME(S) AND ADDRESS(ES)

intentionally left blank

10. SPONSOR/MONITOR'S ACRONYM(S)

11. SPONSOR/MONITOR'S REPORT NUMBER(S)

12. DISTRIBUTION / AVAILABILITY STATEMENT

APPROVED FOR PUBLIC RELEASE; DISTRIBUTION UNLIMITED.

13. SUPPLEMENTARY NOTES

14. ABSTRACT

Atmospheric oxygen absorption bands in observed spectra of boost phase missiles can be used to accurately estimate range from sensor to target. This work compares two oxygen absorption bands in the near-infrared (NIR) and visible (Vis) spectrum, centered at 762 nm and 690 nm, to passively determine range. Spectra were observed from static tests of both surface-to-air missile simulators at 405 m range and a full-scale solid rocket motor at 900 m range. The NIR O_2 band provided range estimates accurate to within 3 % for both tests, while the Vis O_2 band had range errors of 77 % and 15 %, respectively. A Falcon 9 rocket launch at an initial range of 13 km was also tracked and observed for 90 seconds after ignition. The Vis O_2 band provided dynamic range estimates accurate to within 8 % error for the first 30 seconds of tracked observation. The NIR O_2 band, however, overestimated dynamic range with an error no less than 20 %. Additionally, since response time is paramount for interception of boost phase missiles, methods for reducing dependence on line-by-line algorithms to speed calculations are also presented.

15. SUBJECT TERMS

Monocular Passive Ranging, Band Averaged Absorption, Rocket Plume Emission, Atmospheric Absorption Bands, Radiative Transfer Modeling

16. SECURITY CLASSIFICATION OF:			17. LIMITATION OF ABSTRACT	18. NUMBER OF PAGES	19a. NAME OF RESPONSIBLE PERSON
a. REPORT	b. ABSTRACT	c. THIS PAGE			Michael R. Hawks, Lt Col, USAF (ENP)
U	U	U	U	99	19b. TELEPHONE NUMBER *(include area code)* (937) 255-3636, x4828; michael.hawks@afit.edu

Standard Form 298 (Rev. 8–98)
Prescribed by ANSI Std. Z39.18

www.manaraa.com